

Review

Barium Chalcogenide Crystals: A Review

Nadezhda Kostyukova ^{1,*} , Evgenii Erushin ¹ , Andrey Boyko ¹, Galina Shevyrdyaeva ² and Dmitry Badikov ²

¹ Institute of Laser Physics, Siberian Branch of the Russian Academy of Sciences, Ac. Lavrentiev ave. 15B, 630090 Novosibirsk, Russia; render2012@yandex.ru (E.E.)

² High Technologies Laboratory, Kuban State University, Stavropolskaya st. 149, 350040 Krasnodar, Russia; shevyrdyaeva.g@kubsu.ru (G.S.); ntlab@kubsu.ru (D.B.)

* Correspondence: n.duhovnikova@gmail.com

Abstract: In recent decades, new nonlinear optical materials have been actively developed to create coherent tunable light sources in the mid-infrared (mid-IR) part of the spectrum used in a variety of scientific fields. In the present review, the main attention is focused on barium chalcogenide crystals, including their linear and nonlinear optical properties, laser-induced damage threshold (LIDT), and frequency down-conversion.

Keywords: barium chalcogenide; frequency down-conversion; laser-induced damage threshold (LIDT); mid-infrared (mid-IR) range

1. Introduction

The growing significance of mid-IR tunable coherent sources is becoming more apparent due to the constant advancements in modern technologies, medicine, industry, and science. This progress necessitates the use of more precise and reliable tools for diagnostics, control, and measurements. This specific part of the spectrum encompasses the main transparency windows of the atmosphere. These windows exhibit the characteristic absorption lines of vibrational–rotational transitions of various gases, including H₂O, CO₂, CH₄, NO, N₂O, and others [1]. Moreover, the mid-IR range includes transparency regions for many biological objects and compounds of a biological origin, as well as optical and semiconductor materials. As a result, such sources find a wide range of applications, including atmospheric monitoring systems [2,3], noninvasive medical diagnostics [4,5], thermography (thermal imaging) [6], laser surgery [7,8], and various other applications. In various applications, particularly gas analysis applications, the mid-IR range sources listed below are commonly used: CO and CO₂ gas lasers [3,7] along with their frequency-doubled radiation [9,10]; hydrogen fluoride (HF) and deuterium fluoride (DF) chemical lasers [11]; solid-state lasers utilizing crystals doped with transition metals and rare earth ions [12]; III-V diode and IV-VI lead salt diode lasers [13]; tunable quantum cascade lasers (QCLs) [14,15]; and frequency down-converters, like optical parametric oscillators (OPOs) and difference frequency generators (DFGs) [16,17].

The employment of a CO laser enables the discrete tuning of the radiation wavelength within the spectral range spanning from 4.9 μm to 7.5 μm. Furthermore, it is feasible to produce radiation based on transitions of the first vibrational overtone within the spectral range of 2.5–4.2 μm [18]. A discretely tunable CO₂ laser generates radiation within a range of 9.2 μm to 10.6 μm [19]. Using the isotopes of carbon dioxide molecules as an active medium, the spectral range that encompasses the frequencies of the primary lines of a CO₂ laser can be significantly extended to 8.9–12.3 μm [18]. In addressing gas analysis challenges, the feasibility of utilizing CO and CO₂ lasers hinges on the precise alignment of the laser emission lines with the absorption lines of the gases being studied. Since absorption lines of substances may lie between the generation lines of gas lasers, nonlinear frequency converters driven by CO and CO₂ gas lasers are deployed to generate radiation between these lines [20].



Citation: Kostyukova, N.; Erushin, E.; Boyko, A.; Shevyrdyaeva, G.; Badikov, D. Barium Chalcogenide Crystals: A Review. *Photonics* **2024**, *11*, 281. <https://doi.org/10.3390/photonics11030281>

Received: 23 February 2024

Revised: 16 March 2024

Accepted: 18 March 2024

Published: 21 March 2024



Copyright: © 2024 by the authors. Licensee MDPI, Basel, Switzerland. This article is an open access article distributed under the terms and conditions of the Creative Commons Attribution (CC BY) license (<https://creativecommons.org/licenses/by/4.0/>).

The application of HF and DF chemical lasers that produce radiation between 2.7 μm and 5 μm is constrained by the discrete emission spectra, the strong corrosiveness and harmful nature of fluorides, and the requirement for high-voltage power sources [21].

Presently, the wavelength range of radiation produced by lasers utilizing crystals doped with transition metals and rare earth elements is capped at 5 μm [22]. Interband cascade lasers also serve as mid-infrared sources. However, radiation generation beyond 5 μm was achieved at cryogenic temperatures [23,24]. QCLs have the capability to produce radiation within the mid-IR spectrum. The wavelength of the light emitted from these lasers spans from 3.5 to 24 μm [25]. To achieve a broad range of wavelength tuning, multiple QCLs are simultaneously employed within a single enclosure. One notable disadvantage of quantum cascade lasers is the relatively limited beam quality, a characteristic shared with semiconductor lasers.

Frequency down-conversion is a useful method to broaden the operating range of existing lasers. A significant benefit is the potential to develop solid-state laser systems that offer continuous wavelength tuning across a wide spectrum. Although there are numerous nonlinear crystals suitable for OPOs, only a limited selection is commonly employed due to the lack of essential characteristics required to achieve a high output energy and performance. These crucial properties include having a transparency window within the desired spectral region, a high optical quality (with an absorption coefficient below 0.01 cm^{-1}), an appropriate nonlinear coefficient, a laser-induced damage threshold (LIDT) of at least 0.3 J/cm^2 for nanosecond pulses, minimal nonlinear losses and excellent thermo-mechanical characteristics.

Oxide crystals with a regular domain structure, such as PPLN, PPKTP, and PPKTA, are commonly used for OPOs in the 2–5 μm range [26]. When aiming to produce radiation at longer wavelengths, nonoxide semiconductor crystals become essential as their transmission range surpasses that of oxide crystals. Semiconductor crystals have narrower bandgaps compared to oxides, resulting in an increased quadratic susceptibility and a reduced LIDT [27]. The first semiconductor crystal where optical parametric oscillation was first demonstrated was the proustite Ag_3AsS_3 [28]. The main constraint hindering the extensive application of proustite was its low LIDT of 0.21 J/cm^2 (at 1.064 μm , 17.5 ns, 2 Hz, 1000 pulses) [29]. Since the 1990s, there has been significant progress in the field of a periodic pattern of domain orientation in semiconductors, such as GaAs, GaP, InAs, InP, InSb, ZnSe, and others [30,31]. Currently, the development of periodic structures using these materials remains a challenging and pressing technological objective.

Among semiconductor crystals, commercially available crystals, such as the silver thiogallate AgGaS_2 (AGS) [32], the silver selenogallate AgGaSe_2 (AGSe) [33], and the zinc germanium phosphide ZnGeP_2 (ZGP) [34], are frequently used. The technologies for growing and processing these crystals are highly advanced. However, ongoing research efforts focus on improving the optical characteristics of these crystals through the incorporation of dopants during growth or through specific post-growth treatments [35–37]. Among these nonlinear materials, only the AGS crystal is suitable for the frequency down-conversion of the commonly used 1 μm solid-state laser to the mid-IR range. This crystal exhibits transparency within the wavelength range of 0.47 to 13 μm , with a clear transparency limit at approximately 8.5 μm . However, it shows a relatively low LIDT of 0.2 J/cm^2 (1.064 μm , 12 ns, 1 kHz) [38]. To pump frequency down-conversion devices based on ZGP and AGSe crystals, laser radiation sources emitting wavelengths between 1.5 and 2 μm are required [39,40]. The ZGP crystal, which is widely utilized, possesses remarkable properties, including a high quadratic nonlinearity coefficient of approximately 75 pm/V and a high thermal conductivity of 36 W/mK [41]. However, its transmission is quite restricted; it is transparent within the range of 0.72–12.3 μm but exhibits a significant absorption dip at 9.0 μm , making it challenging to utilize this crystal for generating radiation beyond 8–8.5 μm [41], which is similar to AGS. In contrast, the AGSe crystal offers a noticeably broader transmission range (0.71 to 19 μm) [41] compared to its sulfur-containing counter-

part AGS and the ZGP crystal. Furthermore, the AGSe crystal has a relatively lower thermal conductivity of 1 W/mK [42] and a low LIDT of 0.65 J/cm² (2.05 μm, 50 ns, 50 Hz) [43].

The aforementioned points highlight the importance of developing novel nonoxide nonlinear crystals considering their diverse potential applications. The selection of a suitable nonlinear crystal should be based on a comprehensive evaluation of all of its physical properties relevant to the specific requirements of a given task. In applications involving the generation of high-power pulsed or continuous-wave radiation, a critical characteristic of crystals is their high thermal conductivity. Conversely, for applications necessitating a broad spectral range of wavelength tuning, factors such as the transparency range, nonlinear coefficient, and phase-matching conditions are crucial. In scenarios demanding a high pulse energy, such as in laser surgery, it is imperative for the nonlinear crystal to exhibit a high LIDT.

Over the past decade, the attention of researchers has been focused on chalcogenide crystals, including alkali and alkali earth metals such as Li and Ba [44]. Technology has been advanced to grow lithium chalcogenides, such as LiGaTe₂ (LGT), LiInS₂, LiInSe₂, LiGaSe₂, and LiGaS₂ (LGS), as a substitute for the commonly used AGS, AGSe, and ZGP crystals. All ternary chalcogenides containing lithium are classified in the crystallographic class *mm2*, except LGT, which falls into the $\bar{4}2m$ class. These compounds exhibit a relatively wide bandgap, ranging from 2.41 to 3.76 eV [44]. Among these materials, the LGS crystal has gained popularity due to its LIDT of 3.3 J/cm² (at 1.064 μm, 14 ns, 100 Hz) [45] and its compatibility with radiation sources emitting wavelengths below 1 μm, specifically Ti:sapphire laser systems operating at 800 nm for frequency down-conversion in femtosecond and picosecond regimes [46,47]. One method to enhance the properties of nonlinear crystals involves altering their chemical composition by passing from ternary to quaternary compounds [44]. Additionally, recent research efforts have focused on developing novel lithium-containing systems such as Li/Ag In/Ga/Ge/Se/Te. For example, compounds such as Li_xAg_{1-x}InSe₂ and Li_xAg_{1-x}GaSe₂ have been successfully produced and characterized [48,49].

Ba-containing ternary and quaternary chalcogenides have emerged as potential substitutes for AGS, AGSe, and ZGP crystals. In the period from 2009 to 2012, the synthesis of two promising wide-bandgap ternary chalcogenide crystals, BaGa₄S₇ (BGS) [50,51] and BaGa₄Se₇ (BGSe) [52,53], was successfully achieved. These crystals exhibit broad mid-IR transparency ranges, spanning from 0.35 to 12 μm for BGS and from 0.47 to 18 μm for BGSe at 0% transparency. Shortly thereafter, the quaternary barium chalcogenide compounds BaGa₂GeS₆ (BGGs) and BaGa₂GeSe₆ (BGGSe) were produced [54,55]. In 2016, these crystals were grown in large sizes with a high optical quality using the Bridgman–Stockbarger technique [56]. More recently, in 2022, a novel crystal, Ba₂Ga₈GeS₁₆ (B2GGs), was also synthesized [57,58].

The present paper focusses on the optical, nonlinear, and thermo-mechanical properties of the barium compounds listed above. Particular attention will be paid to LIDT research and frequency down-conversion devices based on these crystals.

2. Crystal Growth

2.1. Ternary Chalcogenides

As previously stated, between 2009 and 2012, BGS crystals were grown effectively using the Bridgman–Stockbarger technique [50,51]. At this time, the selenium-based counterpart BGSe was also synthesized in sufficiently large dimensions for the determination of birefringence and dispersion dependence [52,53]. These parameters are crucial to anticipating the characteristics of phase-matching interactions. High-purity raw materials utilized for charge synthesis included 6Ns for Ga, S, and Se, along with 96% purity for Ba. Taking into account the well-established chemical activity of Ba, the synthesis was conducted using graphite and pyrolytic boron nitride (PBN) containers. The initial components were weighed on the basis of the chemical formulas of the desired compositions and then placed into crucibles made of PBN or graphite. These crucibles were then inserted into a quartz

ampule, which was connected to a vacuum system and pumped to a residual pressure of 2×10^{-5} mbar. Subsequently, the ampule was sealed. The temperature within the synthesis furnace was gradually raised to 1150 °C at a speed of 200 °C per h. Subsequently, the ampoule containing the materials was maintained at this temperature for several hours to ensure homogenization. Following this, the synthesis furnace was turned off and allowed to cool down to ambient temperature.

The obtained charge was transferred to the quartz ampule for crystal growth, which had dimensions of 18 mm in diameter and 150 mm in length. The ampule was then evacuated to a residual pressure of 2×10^{-5} mbar and placed in a furnace for crystal growth using the Bridgman–Stockbarger technique. The temperature increased to 1130–1140 °C (BGS) and to 1070–1080 °C (BGSe). In order to prevent the melt from coming into contact with quartz, the inner part of the ampoule was lined with graphite. It was determined that the melting point was 1105 ± 5 °C for BGS and 1050 ± 5 °C for BGSe. Following multiple initial experiments, the most suitable parameters for the growth procedure were established by evaluating the optical properties of the crystals produced: the crystallization rate fell within the interval of 8 ± 2 mm/day, while the temperature gradient in the crystallization area was 20 ± 2 °C/cm. The typical duration of growth is between 12 and 15 days [52]. Images of boules and plates of ternary barium chalcogenide crystals grown by the Bridgman–Stockbarger technique are displayed in Figure 1.



Figure 1. Images of boules, elements, and plates of BGS and BGSe crystals grown by the Bridgman–Stockbarger technique.

Currently, several research teams are growing these crystals using the Bridgman–Stockbarger technique [50,52,53,59]. However, Schunemann et al. also reported the growth of BGS and BGSe crystals using the horizontal gradient freeze technique [60]. In [60,61], the synthesis of single-phase ternary chalcogenide compounds was carried out by combining high-purity elemental starting materials using a two-temperature vapor transport method in sealed, heavy-walled quartz ampoules. The obtained single-phase ingots were placed back into PBN boats, along with oriented seed crystals. Subsequently, the ampule was sealed. The boats and ampoules were then subjected to heating in multi-zone horizontal transparent tube furnaces with an axial temperature gradient of 1–3 °C/cm to melt the charge and partially re-melt the seed crystal. Afterwards, the ampule was gradually cooled to achieve directional solidification at a rate of approximately 0.5 mm per h.

2.2. Quaternary Chalcogenides

The Bridgman–Stockbarger technique is also employed for the growth of quaternary barium chalcogenides [56]. The binary compounds Ga_2S_3 , Ga_2Se_3 , GeS_2 , and GeSe_2 were synthesized at elevated temperatures by combining high-purity chemical elements Ba (98%), Ga (99.999%), Ge (99.999%), S (99.999%), and Se (99.999%) in quartz ampoules under vacuum conditions of 10^{-5} mbar. The BGGSe crystal was produced by synthesizing a mixture of BaS(e) , $\text{Ga}_2\text{S(e)}_3$, and GeS(e)_2 in a graphitized quartz ampoule with a 1:1:1 molar ratio. A similar procedure was followed for the B2GGSe crystal, but with a molar ratio of 2:4:1. The ampoules were then vacuum-sealed (10^{-5} mbar) and placed in a two-zone horizontal furnace, where they were heated to 1050 °C for 36 h. Subsequently,

the resulting melt was maintained at this temperature for an additional 24 h and stirred until complete homogenization was achieved. The melting points of the compositions were assessed through differential thermal analysis. The heating and cooling rate was 30 °C/min. The recorded melting temperatures were 983 °C for BGGSe, 877 °C for BGGSe, and 1008 °C for B2GGS [56,57].

The crystals of the quaternary compositions were grown using the Bridgman–Stockbarger technique in a vertical furnace with a temperature gradient of 10 °C/cm in the crystallization zone, while the melt was elevated to a temperature 30–40 °C higher than the melting point. The growth speed was 6 mm/day, and the crystals exhibit congruent melting behavior. Annealing is not required for these compositions. Photographs showing boules and plates of quaternary barium chalcogenide crystals are presented in Figure 2.

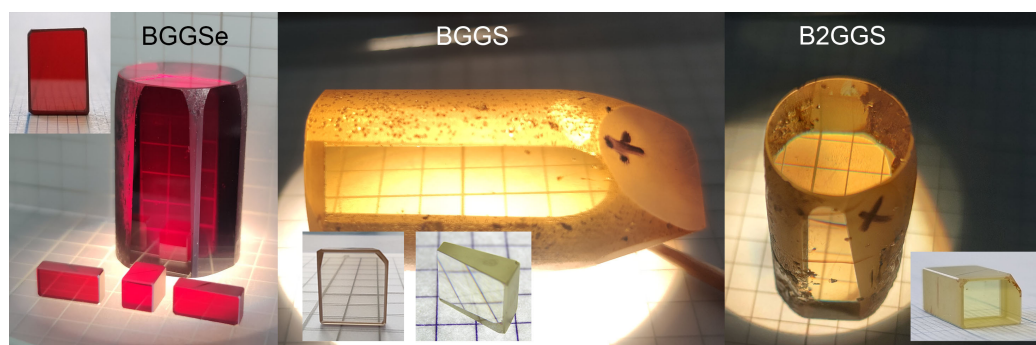


Figure 2. Images of boules, elements, and plates of BGGSe, BGS, and B2GGS crystals grown by the Bridgman–Stockbarger technique.

3. Characterization

3.1. Crystallographic Data

Both Ba-containing ternary compounds exhibit biaxial properties. However, although they have similar chemical compositions, BGS crystallizes in the monoclinic *m* point group, whereas BGGSe belongs to the *mm2* orthorhombic point group as mentioned above. The Ba-containing quaternary compounds are uniaxial. Moreover, BGGSe and BGS are representatives of the trigonal crystal system (crystal class 3), while the new crystal B2GGS belongs to the *6mm* point group (hexagonal crystal system). Table 1 presents data on barium chalcogenides lattice parameters measured using X-ray diffraction by different authors [50,55,61,62].

Table 1. The lattice parameters.

Crystal	Lattice Parameters
BGS	$a = 6.237 \text{ \AA}$, $b = 14.774 \text{ \AA}$, $c = 5.934 \text{ \AA}$ [61] (using the convention $c < a < b$ [63])
BGGSe	$a = 7.6252 \text{ \AA}$; $b = 6.5114 \text{ \AA}$; $c = 14.702 \text{ \AA}$; $\beta = 121.24^\circ$ [50] $a = 14.702 \text{ \AA}$, $b = 6.5114 \text{ \AA}$, $c = 7.6252 \text{ \AA}$, $\beta = 121.24^\circ$ [61] (using the convention $c < a$, b —monoclinic axis [63])
BGGSe	$a = 9.5967 \text{ \AA}$; $c = 8.671 \text{ \AA}$ [55]
BGGSe	$a = 10.0438 \text{ \AA}$; $c = 9.114 \text{ \AA}$ [55]
B2GGS	$a = 10.886 \text{ \AA}$, $c = 11.915 \text{ \AA}$ [62]

3.2. Optical Properties

Ba-containing sulfides have better transmission in the visible region than selenide compounds, and the lowest short-wave cut-off edge of 340 nm possesses a crystal BGS. However, they are only transparent up to 12–12.5 μm at the 0% level. Selenides, in contrast, have longer mid-IR cut-off wavelengths, up to 18 μm. The transmission spectra of 2 mm

thick BGS (black curve), BGGs (red curve), B2GGs (blue curve), BGSe (green curve), and BGGSe (purple curve) plates are given in Figure 3. Transmission spectra of barium chalcogenides were recorded using a Photon RT spectrophotometer in the UV to near IR, whereas in the mid-IR we used an Infracum 801 Fourier transform spectrometer.

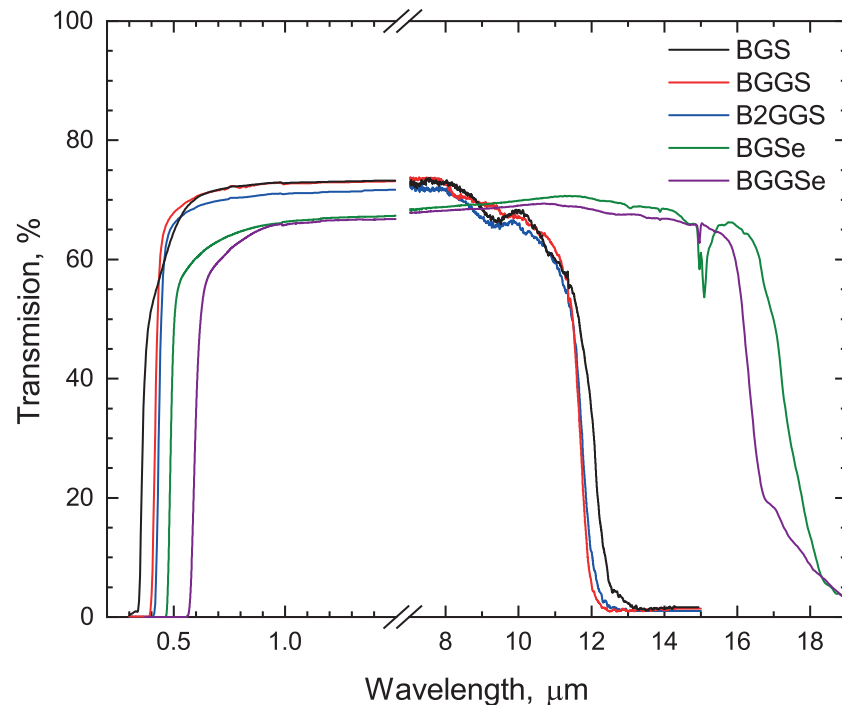


Figure 3. Transmission spectra of 2 mm thick BGS (black curve), BGGs (red curve), B2GGs (blue curve), BGSe (green curve) and BGGSe (purple curve) plates recorded with unpolarized light.

The transparency ranges at the 0% transmission level for plates of BGS, BGGs, and B2GGs with a thickness of 2 mm are 0.34–13.3, 0.38–12.4, and 0.41–12.7 μm , respectively. The sulfides have larger bandgaps compared to the selenides. Specifically, the bandgap values for BGS, BGGs, and B2GGs crystals are 3.59, 3.37, and 3.07 eV, respectively [57,64]. In contrast, the BGSe crystal has a band gap of 2.73 eV, while the BGGSe crystal has a band gap of 2.38 eV [59,64]. At room temperature, for a 2 mm thick BGSe plate, the transparency range at the 0% level is 0.46–18 μm . Yelissev et al. [59] demonstrated that a BGSe plate with a thickness of 200 μm exhibits transparency in the wavelength range of 0.465–22 μm . Additionally, they investigated the variation in the bandgap with temperature. It was observed that when the sample temperature was lowered to 80 K, the bandgap increased to 2.91 eV, with $dE_g/dT = -8.07 \times 10^{-4}$ eV/K. An intense residual absorption peak around 14.5–15 μm in BGSe is similar to those observed in other nonlinear crystals such as AGSe. In [65], the authors investigated the structural characteristics of residual absorption and identified that the absorption bands at approximately 665 cm^{-1} were caused by deformation vibrations of the Ga-O-Ga bonds within the crystal. This phenomenon occurs as a result of the formation of an O substitution defect in the Se (O_{Se}) position during the growth process of the BGSe crystal. Figure 3 illustrates that the BGGSe transmission starts at a wavelength of 0.56 μm and extends up to nearly 18 μm at the 0% level.

3.3. Dispersion Characteristics

The auto-collimation method was used to measure the refractive indices of BGS crystals in the spectral range of 0.42–9.5 μm . Prisms were employed for this purpose, and the resulting data were approximated to the Sellmeier equations [52]. Subsequently, Kato et al. presented improved Sellmeier equations derived from phase-matched nonlinear processes, such as second-harmonic, sum-frequency and difference-frequency generation [66]. These

equations are valid within a wavelength range of 0.633–8.018 μm . This work also presents equations for thermo-optic dispersion.

The initial investigation of the dispersion dependence of the BGSe crystal was conducted using prisms [52,67]. Later, enhanced Sellmeier equations that are obtained through nonlinear frequency conversion were introduced [68,69]. The study [68] investigated the phase-matching conditions by employing the sphere method within the wavelength range of 2–11 μm . To achieve this, a crystal was shaped into a polished sphere with a diameter of 7.55 mm. The temperature-dependent behavior of the refractive indices of the BGSe crystal was investigated within two spectral ranges: 0.546–2.325 μm (25–125 $^{\circ}\text{C}$) [70] and 0.901–14.201 μm (20–120 $^{\circ}\text{C}$) [71]. In study [56], in which the authors first reported the successful growth of large-sized BGGs and BGGSe crystals with good optical quality, the dispersion dependences of both crystals were studied using the minimum deviation of a prism technique. Kato et al. later created improved Sellmeier equations that are applicable to the wavelength range of 0.8–10.6 μm [72,73]. The researchers employed a similar methodology to that used for BGS and BGSe [66,71]. Additionally, they derived thermo-optical dispersion formulas for BGGs and BGGSe crystals [72,74].

Initially, the dispersion characteristics of the B2GGs crystal were studied using a prism [57,58]. Subsequently, the Sellmeier equations were improved through phase-matching processes, and the temperature variations of refractive indices were investigated within the temperature range of 20 to 150 $^{\circ}\text{C}$ [75].

3.4. Nonlinear Optical Characteristics

Table 2 presents the formulas for the effective nonlinearity of barium chalcogenide crystals, which are provided for biaxial crystals in the principal planes of the dielectric frame.

In a BGS crystal, the second-order symmetry axis aligns with the principal dielectric axis x ; the relationship between the crystallographic and dielectric coordinate systems in this crystal can be expressed as $xyz \equiv cab$ given the conditions $n_x < n_y < n_z$ and $c < a < b$. The angle between the optical axis and the principal dielectric z axis, as measured experimentally, is 45.6 $^{\circ}$ [52].

In monoclinic crystals, the b -crystallographic axis always aligns with one of the principal dielectric axes. Experimental results from X-ray, conoscopic, and refractive index measurements indicate that in the case of BGSe, the monoclinic axis $x \equiv b$ is normal to the a - c plane, $z \equiv c$, and the experimental angle between the optical axis and the z -principal dielectric axis Ω is 26.3 $^{\circ}$ [52]. For a dielectric-frame BGSe with orthogonal axes (x, y, z) defined by the relationship $n_x < n_y < n_z$, the x -axis is perpendicular to the mirror plane m . In a study [76], the b -axis was also designated as parallel to the x -axis and the z -axis as parallel to the a -axis. Consequently, the y -axis forms an angle of 31.24 $^{\circ}$ with the c -axis. The same researchers previously observed that the dielectric frame does not rotate around the x -axis based on the wavelength [77]. The orientation of the (x, y, z) axes with respect to the mirror plane m determines the six non-zero and independent components of the second-order dielectric susceptibility tensor, as outlined in Table 2. Detailed discussions on the applicability of the principal dielectric axes system x, y, z to describe components of the nonlinearity tensor instead of the crystallo-physical frame recommended by the standard [63] are presented in [64].

The expressions for the effective nonlinearity of BGGs and BGGSe crystals are provided in the orthogonal right-handed coordinate system x, y, z where $x \equiv a$ and $z \equiv c$, which represents the third-order symmetry axis. Therefore, in this scenario, x, y, z can be viewed as a crystallo-physical frame. The BGGSe components of the nonlinearity tensor are provided in reference [78]. Unfortunately, the data regarding the BGGs crystal have not been published.

The second harmonic generation in the B2GGs crystal was demonstrated in reference [58], where the estimation of the d_{15} component value was detailed. In this research, the a -axis, like in the instances of BGGs and BGGSe, was defined to be parallel to the x -axis, while the z -axis was aligned with the c -axis.

Table 2. The expressions for the effective nonlinearity of barium chalcogenide crystals. The symbols o and e denote the ordinary and extraordinary waves, respectively, in the order of $\lambda_1\lambda_2 - \lambda_3$, where $\lambda_1 \geq \lambda_2 > \lambda_3$; Ω is the angle between the optical axis of the crystal and the Z axis; and θ and φ are the polar and azimuthal angles.

Crystal	Effective Nonlinearity Expressions	d_{il} , pm/V
BGS	x - y : $d_{eff(oo-e)} = d_{32} \sin \varphi$; y - z : $d_{eff(ee-o)} = d_{32} \sin^2 \theta + d_{31} \cos^2 \theta$; x - z , $\theta < \Omega$: $d_{eff(oe-o)} = d_{31} \cos \theta$; x - z , $\theta > \Omega$: $d_{eff(oe-o)} = d_{eff(eo-o)} = d_{31} \cos \theta$;	$d_{15} = d_{31} = 5.1$; $d_{24} = d_{32} = 5.7$; $d_{31} / d_{32} > 0$; @532 nm [51]
BGSe	x - y : $d_{eff(oo-e)} = d_{23} \cos \varphi$; x - y : $d_{eff(oe-e)} = d_{eff(eo-e)} = -d_{15} \sin^2 \varphi - d_{24} \cos^2 \varphi$; y - z , $\varphi = \pm 90^\circ$: $d_{eff(oe-o)} = d_{eff(eo-o)} = \pm d_{16} \cos \theta - d_{15} \sin \theta$; x - z , $\theta < \Omega$: $d_{eff(oo-e)} = d_{24} \sin \theta$; x - z , $\theta < \Omega$: $d_{eff(oe-e)} = d_{eff(eo-e)} = d_{16} \cos^2 \theta + d_{23} \sin^2 \theta$; x - z , $\theta > \Omega$: $d_{eff(oe-o)} = d_{16} \cos^2 \theta + d_{23} \sin^2 \theta$; x - z , $\theta > \Omega$: $d_{eff(oe-o)} = d_{eff(eo-o)} = -d_{24} \sin \theta$;	$d_{21} = d_{16} = 5.3$; $d_{23} = d_{34} = -14.2$; $d_{15} = d_{31} = 1.5$; $d_{24} = d_{32} = -5.0$; $d_{22} = \pm 6.2$; @532 nm [76]
BGGS		$d_{15} = d_{31}$; No data
BGGSe	$d_{eff(ee-o)} = (d_{11} \sin 3\varphi + d_{22} \cos 3\varphi) \cos^2 \theta$; $d_{eff(oe-o)} = d_{eff(eo-o)} = (d_{11} \cos 3\varphi - d_{22} \sin 3\varphi) \cos \theta + d_{31} \sin \theta$;	$d_{15} = d_{31} = 18.3$; $d_{11} = 23.6$; $d_{22} = -18.5$; @5.3 μm [78]
B2GGS	$d_{eff(oo-e)} = d_{15} \sin \theta$;	$d_{15} = d_{24} =$ $d_{31} = d_{32} = 13$; @1.86 μm [57]

Nonlinear absorption and nonlinear refraction occurring in crystals when exposed to intense laser radiation can cause alterations in the transverse intensity profile of the laser beam within the crystal. This can result in self-focusing effects and optical cavity detuning and ultimately decrease the efficiency of frequency down-conversion. Hence, it is crucial to consider these factors when developing optical setups for highly efficient optical parametric oscillators that are tunable in the mid-infrared spectrum.

The nonlinear absorption and nonlinear refraction results shown in Table 3 were obtained through the Z-scan technique introduced by Sheik-Bahae et al. [79]. In the years 2019–2020, Mero et al. measured nonlinear refractive indices (n_2) of several nonlinear crystals, including LGS and BGS crystals, by exposing the samples to femtosecond pulses at a wavelength of 1.028 μm [80,81]. Experiments carried out in identical conditions reveal that the nonlinear refractive index of the BGS crystal is nearly double that of the LGS crystal ($\sim 0.4 \times 10^{-14} \text{ cm}^2/\text{W}$). Both crystals showed a weak dependence of response on the polarization of the laser radiation and the absence of nonlinear absorption at these intensities, and there was no presence of nonlinear absorption at the specified peak intensities. In the study by reference [82], which focused on constructing a picosecond optical parametric amplifier using a BGSe crystal, researchers observed nonlinear absorption within the crystal. This phenomenon initiates at a peak intensity of 1.3 GW/cm^2 and increases further at 2.38 GW/cm^2 .

Table 3 also includes data measured by us and not published before. Nonlinear absorption (β) was observed and measured exclusively in the BGGSe crystal, characterized by the smallest bandgap (2.38 eV), among all the crystals tested, when irradiated by nanosecond pulses at a wavelength of 1.053 μm (245 MW/cm^2). This could be attributed to the close proximity of the laser photon energy $\hbar\omega = 1.18 \text{ eV}$ to half the bandgap energy value $E_g/2 = 1.19 \text{ eV}$ (o-wave). The nonlinear absorption coefficient was measured to be between 1.3 and 2.2 cm/GW . This crystal also demonstrates a higher nonlinear refractive index compared to other crystals of $7.4\text{--}14 \times 10^{-14} \text{ cm}^2/\text{W}$. In our study, nonlinear absorption in the BGSe crystal was not detected at intensities roughly one-tenth of those reported in [82]. BGS and BGGSe crystals exhibit minimum nonlinear refractive indices, approximately $\sim 0.8 \times 10^{-14} \text{ cm}^2/\text{W}$, which aligns well with the data for BGS reported

by Mero et al. [80,81]. We intend to carry out a comprehensive investigation in the upcoming period on the nonlinear absorption and nonlinear refraction of barium chalcogenide crystals. This study will encompass a range of intensities, pulse repetition rates for pulsed lasers, and a CW regime.

Table 3. Nonlinear absorption and nonlinear refraction of barium chalcogenide crystals.

Crystal	Measurement Conditions	$n_2 \cdot 10^{-14}, \text{cm}^2/\text{W}$	$\beta, \text{cm}/\text{GW}$
BGS	1.053 μm ; 5.1 ns; 100 Hz; 700 MW/cm ² ; 2.03 mm long;	0.85	Not observed
	1.028 μm ; 180 fs; 100 Hz and 100 kHz; 8 GW/cm ² ; o- and e-pol., 4.8 mm long; [80]	0.72–0.83	Not observed
	1.028 μm ; 180 fs; 100 Hz and 100 kHz; 2.3 GW/cm ² ; o- and e-pol., 8.3 mm long; [81]	1.0	Not observed
BGSe	1.053 μm ; 5.1 ns; 100 Hz; 245 MW/cm ² ; o- and e-pol.; 2.31 mm long	1.55–1.81	Not observed
	1.064 μm ; 30 ps; 10 Hz; occurs at 1.3 GW/cm ² ; 4 mm long; [82]	No data	Observed
BGGS	1.053 μm ; 5.1 ns; 100 Hz; 700 MW/cm ² ; 2.05 mm long	0.78	Not observed
BGGSe	1.053 μm ; 5.1 ns; 100 Hz; 245 MW/cm ² ; o- and e-pol.; 2.04 mm long	7.4–14	1.3–2.2
B2GGS	1.053 μm ; 5.1 ns; 100 Hz; 700 MW/cm ² ; 2.6 mm long	1.93	Not observed

3.5. Thermophysical Characteristics

The practical use of nonlinear crystals strongly relies on the thermophysical properties of materials. Table 4 presents data regarding the thermal conductivity, thermal diffusivity, and thermal expansion of barium chalcogenide crystals. As far as we know, no such studies have been published for the B2GGS crystal up until now.

Table 4. Thermophysical characteristics of barium chalcogenides along the three crystallographic directions.

Crystal	Thermal Conductivity, $\text{Wm}^{-1}\text{K}^{-1}$			Thermal Diffusivity, mm^2s^{-1}			Thermal Expansion, 10^{-6}K^{-1}					
	a	b	c	a	b	c	a	b	c			
BGS [83]	1.46	1.58	1.68	@323 K	0.74	0.80	0.93	@323 K	No data	No data	No data	
	1.54	1.46	1.52	@373 K	0.66	0.72	0.82	@373 K				
	1.57	1.45	1.44	@423 K	0.64	0.68	0.78	@423 K				
BGSe [84]	0.74	0.64	0.56	@298 K	0.50	0.42	0.38	@298 K	9.24	10.76	11.70	@293–573 K
BGGS [85]	0.91		1.10	@298 K	1.10–0.6		0.9–0.5	@184–473 K	12.1		6.93	@300 K
BGGSe [85]	0.63		0.76	@298 K	0.8–0.4		0.65–0.35	@184–473 K	12.2		3.84	@300 K
B2GGS	No data	No data	No data		No data	No data	No data		No data	No data	No data	

Out of these compounds, the BGS crystal exhibits the highest thermal conductivity, surpassing that of the AGS crystal ($1.143\text{--}1.162 \text{ Wm}^{-1}\text{K}^{-1}$ at 298 K [86] and $1.4\text{--}1.5 \text{ Wm}^{-1}\text{K}^{-1}$ [42]). Selenide compounds exhibit a lower thermal conductivity. Barium selenides have a thermal conductivity that is approximately 30% lower than that of the commonly used sulfide AGSe crystal ($0.95\text{--}1.03 \text{ Wm}^{-1}\text{K}^{-1}$ at 298 K [87] and $1.0\text{--}1.1 \text{ Wm}^{-1}\text{K}^{-1}$ [42]). In the year 2021, the thermal conductivity coefficients for BGGS and BGGSe crystals were reported to be in the ranges of $1.7\text{--}1.95 \text{ Wm}^{-1}\text{K}^{-1}$ and $1.88\text{--}2.17 \text{ Wm}^{-1}\text{K}^{-1}$, respectively, according to [88]. However, subsequent research conducted by the co-authors of the aforementioned study extensively examined the thermo-mechanical properties of these crystals [85]. They concluded that the thermal conductivity values presented in [88] were clearly overestimated and were

accompanied by errors in determining the specific heat capacity. As previously stated, the thermal conductivity of nonlinear crystals is crucial in producing high-average-power radiation sources. Unlike the ZGP crystal ($36 \text{ Wm}^{-1}\text{K}^{-1}$ [41]) utilized in high-power OPOs, barium chalcogenides exhibit a considerably lower thermal conductivity. Nevertheless, their high LIDT, as demonstrated below, coupled with their broad transmission range, makes these crystals highly suitable for generating radiation with a high pulse energy [89] or a wide range of wavelength tuning [90].

3.6. Mechanical Characteristics

Information on the mechanical characteristics of nonlinear crystals is crucial for their widespread use. This knowledge is essential for various processes such as cutting, polishing, cleaning, the anti-reflection coating of optical surfaces, and evaluating the impact of thermal stress. The data in Table 5 provide information on the hardness and Young’s modulus of barium chalcogenide crystals. To our knowledge, no publications have been published on the B2GGS crystal.

Table 5. Hardness and Young’s modulus of of barium chalcogenides.

Crystal	Hardness, GPa	Hardness VHN, kg/mm ²	Young’s Modulus, GPa	Temperature, K	Thermal Drift, nm/s
BGS [91]	6.00	556	80.0	291.75	0.26
BGSe [91]	3.63	336	57.6	289.85	0.33
BGGs [85]	a-cut	4.99	463	293.7	0.3
	c-cut	4.66	432	294.5	0.17
BGGSe [85]	a-cut	4.10	380	294.2	0.19
	c-cut	4.25	394	294.2	0.14
B2GGS	No data	No data	No data	No data	No data

Among these compounds, the BGS crystal demonstrates the greatest hardness, measuring at 6.00 GPa (Vickers hardness number of 556 kg/mm²), and a Young’s modulus of 80.0 GPa [91]. In the first study published in 2009, which focused on the crystal’s growth, a hardness of 327.5 kg/mm² was reported [50]. This difference in hardness could be attributed to the significant advancements in crystal growth technology over the past decade, allowing for the production of more homogeneous crystals with a high optical quality. Barium chalcogenide crystals, whose mechanical properties were studied (refer to Table 5), demonstrate greater hardness levels when compared to AGS (285 kg/mm²) and AGSe (170 kg/mm²) crystals [92].

4. LIDT

The laser-induced damage threshold is a key parameter in optical components as well as in nonlinear crystals. This parameter depends on various factors, such as the wavelength, pulse duration, pulse repetition rate, surface quality, presence of coatings, etc. The LIDT is defined in the ISO 21254 standard as the “highest quantity of laser radiation incident upon the optical component for which the extrapolated probability of damage is zero” [93]. Under the influence of short laser pulses $\tau < 10^{-7}$, damage to the material can occur due to dielectric breakdown and nonlinear (two-photon absorption, self-focusing) and thermal processes, and it can also combine all these components [94,95]. The thermal processes are insignificant for ultrashort pulses of about 10 ps or less. In this case, the damage is prevalent in nonlinear processes such as multi-photon absorption and multi-photon, tunnel, and avalanche ionization [96].

For pulsed sources, the LIDT is defined as the peak-on-axis fluence and expressed in $[\text{J}/\text{cm}^2]$, as this provides the best metric for such sources. There is no need to specifically calculate it to match it to the size of the spot, as a known damage threshold can be applied to any beam diameter [97]. However, in most real transparent optical materials, there is a size dependence of the LIDT associated with the presence of absorbing defects in the material that initiate destruction [98]. The presence of absorbing defects and inclusions, which are

typically found in different amounts in real optical materials, often serves as a primary cause of both surface and bulk damage to the materials, leading to a notable reduction in the threshold intensity. Typically, such defects refer to various irregularities, such as cracks, scratches, dents, or contamination, due to which the optical element fails more quickly or at a significantly lower power density than originally intended. As the beam size increases, the probability that a defect will be present in the irradiated area increases noticeably, resulting in a reduced LIDT compared to situations with smaller beam sizes.

Damage caused by continuous-wave (CW) lasers is typically due to thermal effects occurring by absorption in the optical coatings or substrate and is expressed in the peak-on-axis intensity measured in $[W/cm^2]$. The effective size of the Gaussian beam is also related to the energy density. As this density increases, most of the beam width is energetic enough to cause laser damage. According to the ISO 21254 standard, the effective area of a Gaussian beam is defined as $\pi\omega^2/2$. To recalculate the LIDT value from one pulse duration to another, the following equation is used [99]:

$$LIDT(\tau_2) \approx LIDT(\tau_1) \times \sqrt{\frac{\tau_2}{\tau_1}}, \tag{1}$$

where τ is the pulse duration. It is important to emphasize that this equation is applicable for pulse durations ranging from 1 to 100 ns and variations in pulse duration should not exceed threefold.

Table 6 shows the LIDT of barium chalcogenide crystals under the influence of radiation sources of various durations, wavelengths, and pulse repetition rates. All values are expressed in terms of the peak-on-axis fluence, with the exception of the data for the femtosecond source. Some data, for a more visual comparison, were scaled using the formula above; for more detailed information, we recommend reference to the relevant publications.

Table 6. LIDT of barium chalcogenide crystals.

Wavelength	10 μm	2 μm	1 μm	
Pulse Duration	ns	ns	fs	
BGS	52.4 J/cm ² (9.58 μm , 100 ns, 1 Hz) [83]	10 J/cm ² (2.1 μm , 15 ns, 1 Hz) * [83]	2.4 J/cm ² (1.064 μm , 15 ns, 1 Hz) [50] 3.7/2.9 J/cm ² (1.064 μm , 14/1 ns, 0.1/0.5 kHz) [51] 7.4/6.4 J/cm ² (1.053 μm , 5.1 ns, 0.1/1 kHz) [100]	
BGSe	36.6 J/cm ² (10.6 μm , 100 ns, 1 Hz) [101]	4.8/3.3/2.1 J/cm ² (2.091 μm , 15 ns, 2/5/10 kHz) [102] 2.46 J/cm ² (2.091 μm , 15 ns, 0.5 kHz) * [103] 1.37 J/cm ² (2.091 μm , 15 ns, 0.5 kHz) * [104]	81 GW/cm ² (2.4 μm , 28 fs, 69 MHz) [105] 2/1.4/1.1 J/cm ² (1.053 μm , 5.1 ns, 0.1/0.5/1 kHz) * [106] 2.9/2.9/2.6 J/cm ² (1.053 μm , 8.3 ns, 0.1/0.15/0.2 kHz) * [107] 1.4/1 J/cm ² (1.064 μm , 14/1 ns, 0.1/0.5 kHz) [90] 5.6 J/cm ² (1.064 μm , 5 ns, 1 Hz) [84]	0.18 J/cm ² (1.064 μm , 30 ps, 10 Hz) [108]
Doped BGSe		6.6/5.1/2.5 J/cm ² (2.091 μm , 15 ns, 2/5/10 kHz) [102]	2.5/2.3/2.3/2 J/cm ² (1.053 μm , 5.1 ns, 0.1/0.5/1/2 kHz) * [109]	
BGGS	14 J/cm ² (10.6 μm , 100 ns, 1 Hz) [56]		6.8/7 J/cm ² (1.053 μm , 5.1 ns, 0.1/1 kHz) [100]	
B2GGS			6.9/7 J/cm ² (1.053 μm , 5.1 ns, 0.1/1 kHz) [110]	
BGGSe	11 J/cm ² (10.6 μm , 100 ns, 1 Hz) [56]	6.5/4.3/2.7 J/cm ² (2.091 μm , 15 ns, 2/5/10 kHz) [102]	1.9/1.6/1.3 J/cm ² (1.053 μm , 5.1 ns, 0.1/0.5/1 kHz) * [106]	

* Scaled data. Refer to the relevant publications for more detailed information.

BGSe crystals exhibit cleavage planes, which cannot be eliminated by annealing because of their connection with the features of the crystal structure. By varying the composition of additives used to grow BGSe crystals in the laboratory of advanced technologies at Kuban State University, it was feasible to reduce the occurrence of this phenomenon. The composition of the sample was modified by the isomorphic insertion of Ga₂Se₃ in amounts of up to 7.8 mol.%. The LIDT of BGSe crystals, both in their pure form and with a

modified composition, was evaluated using nanosecond pulses at 2 μm and 1 μm [102,109]. According to data from [102], the damage threshold of modified BGSe was approximately 30% higher at pulse repetition rates of 2 kHz and 5 kHz, but this difference decreased to 16% at a higher pulse repetition rate (10 kHz). A similar result was obtained in a study [109] where the LIDT of the modified BGSe was approximately 24% higher than that of the nominally pure BGSe.

In general, all barium chalcogenide crystals considered demonstrate a high LIDT. Particularly, barium sulfide crystals have an LIDT that is more than three times higher than their selenium-containing counterparts, indicating their potential for applications requiring high peak energy. Selenium-containing crystals are also known for their increased nonlinearity and broader transparency range, making them appealing for addressing spectroscopic challenges.

5. Frequency Down-Conversion to the Mid-IR Range

As previously stated, barium chalcogenide crystals show great potential for nonlinear conversion due to several characteristics, such as their transmission range, LIDT, and effective nonlinearity coefficient. This section of the article focuses on the use of these crystals for frequency down-conversion to the mid-IR range. Table 7 presents examples of utilizing the barium chalcogenide crystals for frequency down-conversion to the mid-IR range, along with the resulting radiation properties.

5.1. BGS

To our knowledge, among all barium sulfide compounds, only the BGS crystal was used for frequency down-conversion, being the first one to be successfully grown. BGS was the first barium chalcogenide crystal used for nanosecond OPO applications [111]. A Nd:YAG laser was employed as the pumping source, producing pulses around 7.5 ns at a rate of 10 Hz at a wavelength of 1.064 μm . The developed source produced idler pulses less than 6 ns, with energies reaching up to 0.5 mJ at a wavelength of 6.217 μm and an average power of around 50 mW. Optical parametric amplifiers using ultrashort pulses (ps and fs) were successfully demonstrated in this crystal at a later date, specifically in 2020 [112,113].

In [113], the first demonstration of a mid-IR optical parametric amplifier (OPA) was published. The BGS-OPA was pumped by a Nd:YAG laser with a pulse duration of 30 ps at 1064 nm and 10 Hz. Achieving a maximum idler pulse energy of approximately 130 μJ at 7.25 μm required a pump energy of around 6.9 mJ, resulting in a pump-to-idler quantum conversion efficiency of about 13%. The wavelength tuning was demonstrated in the 6.3–8.8 μm spectral range. In reference [112], an OPA was showcased with pumping by a Yb:KGd(WO₄)₂ laser operating at 1028 nm with a pulse duration of 180 fs and a rate of 100 kHz. The average output power was measured at 59 mW at 10 μm and 81 mW at 8.1 μm . The tuning of the wavelength was demonstrated in the range of 7.6–11.5 μm .

5.2. BGSe

Currently, the BGSe crystal stands out as one of the most extensively researched among all barium chalcogenides. Researchers have successfully utilized this crystal to develop OPOs, OPAs, and DFGs with varying pump wavelengths and pulse durations, along with achieving difference frequency generation in a CW regime. In 2016, we presented the first nanosecond OPO using a BGSe crystal pumped by a 1 μm laser [114]. When using the I-type interaction, the idler wavelength exhibited a tuning range of 2.93–9.3 μm , while for the II type, it was 5–5.4 μm . The peak energy reached 4–10 μJ at a pulse repetition rate of 100 Hz within the 4–5 μm range. Subsequently, in our study [90], the use of a pump laser with an increased pulse energy and the use of crystals of superior optical characteristics led to the achievement of an unprecedented wide tuning range of 2.7–17 μm for BGSe-I and 3.6 to 9.6 μm for BGSe-II. The maximum idler wave energy generated by an OPO utilizing BGSe-II reached 4.7 mJ at a 5.3 μm wavelength, while for an OPO based on BGSe-I, the maximum energy output was 3.7 mJ at a 7.2 μm wavelength, using a pump energy of

63 mJ and a pulse repetition rate of 100 Hz. An extremely high OPO output energy was, 21.5 mJ at 3816 nm with the I type of interaction and a repetition rate of 20 Hz [89]. Also, using a nanosecond Nd:YAG laser as a pump source, an intracavity mixing of the signal (1.85 μm) and idler (2.51 μm) of an Rb:PPKTP OPO in the BGSe crystal was realized [115]. An output pulse energy of approximately 0.7 mJ is produced at ~7 μm with a repetition rate of 100 Hz. The tuning of the mid-IR radiation is implemented through the heating of the Rb:PPKTP crystal.

Table 7. Frequency down-conversion devices based on barium chalcogenide crystals.

Crystal Type, (θ, φ)	Device Type	Length, mm	Pump Source	Pulse Duration and Rep. Rate	Tuning Range	Energy/Power		
BGS I type (9.2°, 0°) [111]	OPO	14.1	Nd:YAG, 1064 nm	8 ns 100 Hz	5.5–7.3 μm	0.5 mJ @6.2 μm		
BGS I type (12.5°, 0°) [113]	OPA	15		30 ps 10 Hz	6.3–8.8 μm	66 μJ @6.3 μm		
BGS I type (13.1°, 0°) [112]	OPA	8.3	Yb:KGd(WO ₄) ₂ , 1028 nm	180 fs 100 Hz	7.6–11.5 μm	59 mW @10 μm 81 mW @8 μm.		
BGSe-I type (45°, 0°) [114]	OPO	11.8	Nd:YLF, 1053 nm	15 ns 100 Hz	2.9–9.3 μm	4–10 μJ @4–5 μm		
BGSe-I type (45°, 0°) [107]	OPO	11.8			2.6–10.4 μm	45 μJ @3.3 μm		
BGSe-II type (33°, 90°) [114]	OPO	10			5–5.4 μm	14 μJ @8.1 μm		
BGSe-I type (46°, 0°) [90]	OPO	14.6			2.7–17 μm	3.7 mJ @7.2 μm		
BGSe-II type (33.5°, 90°) [90]	OPO	13.6			8 ns 10 Hz	3.6–9.6 μm	4.7 mJ @5.3 μm	
BGSe-I type (53.4°, 0°) [116]	OPO	18.8			8 ns 10 Hz	4.1–4.5 μm	1.92 mJ @4.3 μm	
BGSe-I type (54.7°, 0°) [117]	OPO	17.3			16 ns 10 Hz	3.1–5.2 μm	2.56 mJ @4.1 μm	
BGSe-I type (53.2°, 0°) [118]	OPO	10			6.7 ns 10 Hz		1.03 mJ @4.3 μm	
BGSe-I type (55.9°, 0°) [89]	OPO	16			Nd:YAG, 1064 nm	11.4 ns 20 Hz	3.6–3.8 μm	21.5 mJ @3.8 μm
BGSe-I type (42.5°, 0°) [119]	OPO	15			10 ns 10 Hz	8–14 μm	1.05 mJ @11 μm	
BGSe-I type (56.3°, 0°) [120]	OPO	15	13 ns 1 Hz	±5 nm	0.49 mJ @3.5 μm			
BGSe-I type (55.3°, 0°) [121]	OPO	15	11.6 ns 300 Hz	3.2–4.2 μm	1.03 W @3.7 μm			
BGSe-I type (42.5°, 0°) [122]	OPO	16	13.6 ns 250 Hz	3.42–4.73 μm	1.3 mJ @4.1 μm			
BGSe-I type (53.2°, 0°) [123]	OPO	15	13.7 ns 500 Hz		1.52 mJ @4.4 μm			
BGSe-I type (56.3°, 0°) [124]	OPO			13 ns 1 Hz	2.76–4.64 μm			
BGSe-I type (47.1°, 0°) [125]	OPO	25		18 ns 10 Hz		6.8 mJ @6.45 μm		
BGSe-I type (46°, 0°) [115]	DFG	14.6	OPO, 1.85 + 2.51 μm	8 ns 10 Hz	7–8.2 μm	711 μJ @7 μm		
BGSe I type (40.8°, 0°) [103]	OPO	30		27 ns 500 Hz	4.3–5.2 μm	1.47 mJ @4.4 μm		
BGSe-II type (6°, 90°) [104]	OPO	30		16 ns 1 kHz	8–9 μm	314 μJ @8.9 μm		
BGSe-II type (23.5°, 90°) [126]	OPO	33	Ho:YAG, 2091 nm	29.3 ns 1 kHz	3.82–4 μm	520 μJ @3.94 μm		
BGSe-I type (40.8°, 0°) [127]	OPO	30		28 ns 1 kHz	4.5–5.3 μm	1.8 mJ @4.5 μm		
BGSe-I type (39.4°, 0°) [128]	OPO	31	Cr, Er:YSGG, 2.79 μm	21 ns 10 Hz	5.6–9.5 μm	3.5 mJ @5 μm		
BGSe-I type (45°, 0°) [129]	DFG	8	Yb:YAG, 1030 nm	2 ps 10 Hz	6.5–8.6 μm	60 μJ @7 μm		
BGSe I type (54.7°, 0°) [108]	OPA	8			3–5 μm	830 μJ @3.9 μm		
BGSe I type (44°, 0°) [67]	OPA	8	Nd:YAG, 1064 nm	30 ps 10 Hz	6.4–11 μm	38 μJ @11 μm		
BGSe-I type (40.2°, 0°) [82]	OPA	10			8–14 μm	140–230 μJ		
BGSe-I type (47°, 0°) [130]	OPA	10	Yb:KGW, 1030 nm	290 fs 50 kHz	3.7–17 μm	10 mW @16 μm		
BGSe [131]	OPA	1	Yb:YAG, 1.03 μm + 1.15–1.8 μm	550 fs 10 kHz	2.5–10 μm	6 μJ @3 μm		
BGSe-I type (67°, 0°) [132]	DFG	15	Ti:sapphire, 730–970 nm	CW	3.2–7.92 μm	1.41 μW @5 μm		
BGGSe II type (27.5°, 0°) [133]	OPO	9.3	cascaded OPO, 1.85 + 2.51 μm	8 ns 10 Hz	4.4–13 μm	750 μJ @8 μm		
BGGSe II type (27.5°, 0°) [134]	OPO	9.3	cascaded OPO, 1.95 + 2.55 μm	8 ns 100 Hz	6.6–11.3 μm	1.45 mJ @8.2 μm		
BGGSe I type (25°, 30°) [135]	DFG	2.6	mode-locked Er:fiber oscillator	59 fs 100 MHz	5.8–8.5 μm	21 pJ		
BGGSe I type (30°, 28°) [136]	DFG	4.4	SPOPOs, 1035 nm	130 fs 40 MHz	up to 10 μm	54 mW		

In the case of nanosecond OPOs utilizing BGSe, longer-wavelength pump sources were also employed, including a Ho:YAG laser operating at 2.09 μm [103,127] and a Cr, Er:YSGG laser operating at 2.79 μm [128]. In the study by Yang et al. [127], there was a peak output power of 5.12 W with a pump power of 28 W for a Ho:YAG laser system. This output power consisted of 3.44 W of signal wave at 3.9 μm and 1.68 W of idler wave at 4.5 μm.

In 2013, Yang et al. successfully demonstrated a picosecond OPA based on a BGSe-I crystal for the first time [108]. The pump source utilized was a mode-locked Nd:YAG laser system emitting at 1064 nm with a pulse duration of 30 ps and operating at a repetition rate of 10 Hz. They achieved a quantum conversion efficiency of 56% from 1064 nm to 3.9 μm, resulting in a maximum output energy of 830 μJ at 3.9 μm. Additionally, they also presented a tuning curve that spans 3 to 5 μm. Subsequently, the authors illustrated the ability to tune the wavelength within the 8–14 μm range with an energy output ranging from 140 to 230 μJ [82]. Tian et al. successfully demonstrated the first tunable femtosecond mid-IR OPA using a BGSe crystal, offering an exceptionally wide spectral range from 3.7 to 17 μm [130]. The OPA is pumped by a Yb:KGW laser at 1030 nm, delivering pulses of a 250 fs duration at a rate of 50 kHz. At a wavelength of 16 μm with a 290 fs pulse duration, the OPA achieves

a maximum output power of 10 mW, corresponding to a quantum conversion efficiency of 5%.

Although the thermal conductivity of the BGSe crystal is not too large, in 2019 a CW DFG was demonstrated for the first time [132]. This was achieved by mixing a CW Ti:sapphire laser with a CW Nd:YAG laser in a 15 mm long BGSe crystal (I type). The experiment resulted in a tunable range from 3.15 to 7.92 μm , with a maximum DFG power of 1.41 μW recorded at 5 μm .

5.3. BGGSe

The employment of the quaternary barium chalcogenide BGGSe for frequency down-conversion into the mid-IR was demonstrated in [133] for the first time. The experimental setup was similar to the one described in [115], although in the second stage an OPO was used instead of a DFG. The wavelength tuning range achieved in this setup was between 4 and 13 μm at 100 Hz, delivering a peak energy of 750 μJ at around 8 μm . Later, the configuration was upgraded by incorporating a selective element, a volume Bragg grating (VBG), into the first stage. The highest energy attained around 8 μm is 1.1 mJ with a line width of approximately 20 cm^{-1} and a pulse duration of ~ 7 ns. The total conversion efficiencies from 1 to 8 μm for the broad spectrum and with VBG are 31% and 23%, respectively.

The BGGSe crystal was employed for a femtosecond DFG [135,136]. In [136], the authors achieved wavelength tuning down to 10 μm with a maximum internal quantum efficiency of 45%. Research carried out by Elu et al. [135] demonstrated that a BGGSe DFG produces a pulse energy of 21 pJ at 100 MHz in a spectral range of 5.8 to 8.5 μm . The results unveiled the electric field of the carrier-envelope-phase stable pulse duration of 91 fs, which corresponds to fewer than four optical cycles.

This crystal was also utilized for frequency up-conversion to the mid-IR range. The sum frequency generation within the CO laser cavity was realized using the BGGSe crystal [137]. The laser system functioned at the same time in two spectral regions: the fundamental band of the CO laser (4.9–6.0 μm) and its band of sum frequencies (2.45–2.95 μm). Various configurations of the laser cavity were evaluated. The maximum powers of the laser pulses in the fundamental and sum frequency bands were 2 kW and 10 W, respectively.

6. Conclusions

This review focuses on Ba-containing ternary (BGS and BGSe) and quaternary (BGGSe, BGGSe, and B2GGSe) chalcogenides. With the exception of thermal conductivity, these crystals seem to outperform the commonly used AGS and AGSe crystals. All of the crystals discussed exhibit a high LIDT, while sulfide crystals demonstrate an LIDT greater than 3 times that of their selenium-containing counterparts, suggesting their suitability for applications requiring a high peak energy. However, selenides are recognized for their enhanced nonlinearity and wider transparency range, making them attractive for spectroscopic tasks. Currently, the most popular crystals are BGS, BGSe, and BGGSe. These crystals have been used effectively by researchers to create OPOs, OPAs, and DFGs with different pump wavelengths and pulse durations. The outcomes of utilizing crystals in frequency down-conversion devices suggest that barium chalcogenide crystals could emerge as a promising nonlinear crystal for generating mid-IR in the femtosecond, picosecond, and nanosecond regimes with an exceptionally broad tuning spectral range.

Author Contributions: Conceptualization, N.K. and E.E.; investigation, N.K., E.E., A.B., G.S. and D.B.; writing—original draft preparation, N.K., E.E. and D.B.; writing—review and editing, N.K., E.E., A.B., G.S. and D.B.; funding acquisition, N.K. All authors have read and agreed to the published version of the manuscript.

Funding: This study was carried out on the State Assignment of ILP SB RAS FWGU-2021-0010.

Institutional Review Board Statement: Not applicable.

Informed Consent Statement: Not applicable.

Conflicts of Interest: The authors declare no conflicts of interest.

Abbreviations

The following abbreviations are used in this manuscript:

LIDT	Laser-induced damage threshold
mid-IR	Mid-infrared
HF laser	Hydrogen fluoride laser
DF laser	Deuterium fluoride laser
QCL	Quantum cascade laser
OPO	Optical parametric oscillator
DFG	Difference frequency generator
OPA	Optical parametric amplifier
AGS	Silver thiogallate, AgGaS ₂
AGSe	Silver selenogallate, AgGaSe ₂
ZGP	Zinc germanium phosphide, ZnGeP ₂
LGT	LiGaTe ₂
LGS	LiGaS ₂
BGS	BaGa ₄ S ₇
BGSe	BaGa ₄ Se ₇
BGGS	BaGa ₂ GeS ₆
BGGSe	BaGa ₂ GeSe ₆
B2GGS	Ba ₂ Ga ₈ GeS ₁₆
PPLN	Periodically poled lithium niobate
PPKTP	Periodically poled potassium titanyl phosphate
PPKTA	Periodically poled potassium titanyl arsenate
PBN	Pyrolytic boron nitride
VHN	Vickers hardness number
CW	Continuous wave
VBG	Volume Bragg grating

References

- Rothman, L.; Gordon, I.; Babikov, Y.; Barbe, A.; Chris Benner, D.; Bernath, P.; Birk, M.; Bizzocchi, L.; Boudon, V.; Brown, L.; et al. The HITRAN2012 molecular spectroscopic database. *J. Quant. Spectrosc. Radiat. Transf.* **2013**, *130*, 4–50. [\[CrossRef\]](#)
- Harren, F.J.; Mandon, J.; Cristescu, S.M. Photoacoustic Spectroscopy in Trace Gas Monitoring. In *Encyclopedia of Analytical Chemistry*; John Wiley & Sons, Ltd.: Hoboken, NJ, USA, 2012. [\[CrossRef\]](#)
- Schilt, S.; Thévenaz, L.; Niklès, M.; Emmenegger, L.; Hüglin, C. Ammonia monitoring at trace level using photoacoustic spectroscopy in industrial and environmental applications. *Spectrochim. Acta Part A Mol. Biomol. Spectrosc.* **2004**, *60*, 3259–3268. [\[CrossRef\]](#)
- Kistenev, Y.V.; Borisov, A.V.; Kuzmin, D.A.; Penkova, O.V.; Kostyukova, N.Y.; Karapuzikov, A.A. Exhaled air analysis using wideband wave number tuning range infrared laser photoacoustic spectroscopy. *J. Biomed. Opt.* **2017**, *22*, 017002. [\[CrossRef\]](#)
- Litvinova, K.S.; Rafailov, I.E.; Dunaev, A.V.; Sokolovski, S.G.; Rafailov, E.U. Non-invasive biomedical research and diagnostics enabled by innovative compact lasers. *Prog. Quantum Electron.* **2017**, *56*, 1–14. [\[CrossRef\]](#)
- Ventura, A.; Slimen, F.B.; Lousteau, J.; White, N.; Masoudi, A.; Janicek, P.; Poletti, F. Flexible Mid-IR fiber bundle for thermal imaging of inaccessible areas. *Opt. Express* **2019**, *27*, 20259–20272. [\[CrossRef\]](#) [\[PubMed\]](#)
- Aleĭnikov, V.S.; Belyaev, V.P.; Devyatkov, N.D.; Klimentko, V.I.; Mamedli, L.D.; Masychev, V.I.; Sysoev, V.K. Applications of a carbon monoxide laser in surgery. *Sov. J. Quantum Electron.* **1983**, *13*, 1304. [\[CrossRef\]](#)
- Edwards, G.S.; Pearlstein, R.D.; Copeland, M.L.; Hutson, M.S.; Latone, K.; Spiro, A.; Pasmanik, G. 6450 nm wavelength tissue ablation using a nanosecond laser based on difference frequency mixing and stimulated Raman scattering. *Opt. Lett.* **2007**, *32*, 1426–1428. [\[CrossRef\]](#)
- Romann, A.; Sigrist, M.W. Photoacoustic gas sensing employing fundamental and frequency-doubled radiation of a continuously tunable high-pressure CO₂ laser. *Appl. Phys. B* **2002**, *75*, 377–383. [\[CrossRef\]](#)
- Ionin, A.A.; Guo, J.; Zhang, L.M.; Xie, J.J.; Andreev, Y.M.; Kinyayevsky, I.O.; Klimachev, Y.M.; Kozlov, A.Y.; Kotkov, A.A.; Lanskiĭ, G.V.; et al. Mode-locked CO laser frequency doubling in ZnGeP₂ with 25% efficiency. *Laser Phys. Lett.* **2011**, *8*, 723. [\[CrossRef\]](#)
- Patel, B.C.M.; Rickwood, K.R. Morphological changes induced by short pulse hydrogen fluoride laser radiation on dental hard tissue and restorative materials. *Lasers Surg. Med.* **1997**, *21*, 1–6. [\[CrossRef\]](#)

12. Sorokina, I.T. Broadband Mid-Infrared Solid-State Lasers. In *Mid-Infrared Coherent Sources and Applications*; Ebrahim-Zadeh, M., Sorokina, I.T., Eds.; Springer: Dordrecht, The Netherlands, 2008; pp. 225–260. [[CrossRef](#)]
13. Tacke, M. New developments and applications of tunable IR lead salt lasers. *Infrared Phys. Technol.* **1995**, *36*, 447–463. [[CrossRef](#)]
14. Genner, A.; Martín-Mateos, P.; Moser, H.; Lendl, B. A Quantum Cascade Laser-Based Multi-Gas Sensor for Ambient Air Monitoring. *Sensors* **2020**, *20*, 1850. [[CrossRef](#)] [[PubMed](#)]
15. Sherstov, I.; Kolker, D.; Vasiliev, V.; Pavlyuk, A.; Miroshnichenko, M.; Boyko, A.; Kostyukova, N.; Miroshnichenko, I. Laser photo-acoustic methane sensor (7.7 μm) for use at unmanned aerial vehicles. *Infrared Phys. Technol.* **2023**, *133*, 104865. [[CrossRef](#)]
16. Kostyukova, N.Y.; Kolker, D.B.; Zenov, K.G.; Boyko, A.A.; Starikova, M.K.; Sherstov, I.V.; Karapuzikov, A.A. Mercury thiogallate nanosecond optical parametric oscillator continuously tunable from 4.2 to 10.8 μm . *Laser Phys. Lett.* **2015**, *12*, 095401. [[CrossRef](#)]
17. Malara, P.; Maddaloni, P.; Gagliardi, G.; Natale, P.D. Combining a difference-frequency source with an off-axis high-finesse cavity for trace-gas monitoring around 3 μm . *Opt. Express* **2006**, *14*, 1304–1313. [[CrossRef](#)] [[PubMed](#)]
18. Basov, N.G.; Ionin, A.A.; Kotkov, A.A.; Kurnosov, A.K.; McCord, J.E.; Napartovich, A.P.; Seleznev, L.V.; Turkin, N.G.; Hager, G.D. Pulsed laser operating on the first vibrational overtone of the CO molecule in the 2.5–4.2- μm range: 1. Multifrequency lasing. *Quantum Electron.* **2000**, *30*, 771. [[CrossRef](#)]
19. Wittman, W.J. *The CO₂ Laser*; Springer: Berlin/Heidelberg, Germany, 1987; p. 311. [[CrossRef](#)]
20. Budilova, O.; Ionin, A.; Kinyaevskiy, I.; Klimachev, Y.; Kotkov, A.; Kozlov, A. Ultra-broadband hybrid infrared laser system. *Opt. Commun.* **2016**, *363*, 26–30. [[CrossRef](#)]
21. Boreysho, A.S. High-power mobile chemical lasers. *Quantum Electron.* **2005**, *35*, 393. [[CrossRef](#)]
22. Mirov, S.B.; Moskalev, I.S.; Vasilyev, S.; Smolski, V.; Fedorov, V.V.; Martyshkin, D.; Peppers, J.; Mirov, M.; Dergachev, A.; Gapontsev, V. Frontiers of Mid-IR Lasers Based on Transition Metal Doped Chalcogenides. *IEEE J. Sel. Top. Quantum Electron.* **2018**, *24*, 1601829. [[CrossRef](#)]
23. Bewley, W.W.; Canedy, C.L.; Kim, C.S.; Kim, M.; Merritt, C.D.; Abell, J.; Vurgaftman, I.; Meyer, J.R. Continuous-wave interband cascade lasers operating above room temperature at $\lambda = 4.7\text{--}5.6 \mu\text{m}$. *Opt. Express* **2012**, *20*, 3235–3240. [[CrossRef](#)]
24. Li, L.; Ye, H.; Jiang, Y.; Yang, R.Q.; Keay, J.C.; Mishima, T.D.; Santos, M.B.; Johnson, M.B. MBE-grown long-wavelength interband cascade lasers on InAs substrates. *J. Cryst. Growth* **2015**, *425*, 369–372. [[CrossRef](#)]
25. Vitiello, M.S.; Scalari, G.; Williams, B.; Natale, P.D. Quantum cascade lasers: 20 years of challenges. *Opt. Express* **2015**, *23*, 5167–5182. [[CrossRef](#)] [[PubMed](#)]
26. Vodopyanov, K. Pulsed Mid-IR Optical Parametric Oscillators. In *Solid-State Mid-Infrared Laser Sources*; Sorokina, I.T., Vodopyanov, K.L., Eds.; Springer: Berlin/Heidelberg, Germany, 2003; pp. 144–183. [[CrossRef](#)]
27. Jackson, A.; Ohmer, M.; LeClair, S. Relationship of the second order nonlinear optical coefficient to energy gap in inorganic non-centrosymmetric crystals. *Infrared Phys. Technol.* **1997**, *38*, 233–244. [[CrossRef](#)]
28. Ammann, E.O.; Yarborough, J.M. Optical parametric oscillation in proustite. *Appl. Phys. Lett.* **1970**, *17*, 233–235. [[CrossRef](#)]
29. Hanna, D.; Luther-Davies, B.; Rutt, H.; Smith, R.; Stanley, C. Q-switched laser damage of infrared nonlinear materials. *IEEE J. Quantum Electron.* **1972**, *8*, 317–324. [[CrossRef](#)]
30. Angell, M.J.; Emerson, R.M.; Hoyt, J.L.; Gibbons, J.F.; Eyres, L.A.; Bortz, M.L.; Fejer, M.M. Growth of alternating (100)/(111)-oriented II-VI regions for quasi-phase-matched nonlinear optical devices on GaAs substrates. *Appl. Phys. Lett.* **1994**, *64*, 3107–3109. [[CrossRef](#)]
31. Ye, H.; Kumar, S.C.; Wei, J.; Schunemann, P.G.; Ebrahim-Zadeh, M. Singly-resonant pulsed optical parametric oscillator based on orientation-patterned gallium phosphide. *Opt. Lett.* **2018**, *43*, 2454–2457. [[CrossRef](#)] [[PubMed](#)]
32. Fan, Y.X.; Eckardt, R.C.; Byer, R.L.; Route, R.K.; Feigelson, R.S. AgGaS₂ infrared parametric oscillator. *Appl. Phys. Lett.* **1984**, *45*, 313–315. [[CrossRef](#)]
33. Boyko, A.A.; Kostyukova, N.Y.; Marchev, G.M.; Pasiskevicius, V.; Kolker, D.B.; Zukauskas, A.; Petrov, V. Rb:PPKTP optical parametric oscillator with intracavity difference-frequency generation in AgGaSe₂. *Opt. Lett.* **2016**, *41*, 2791–2794. [[CrossRef](#)]
34. Antipov, O.; Eranov, I.; Kositsyn, R. 10-W mid-IR optical parametric oscillators based on ZnGeP₂ elements pumped by a fibre-laser-pumped Ho: YAG Laser. Experimental and numerical study. *Quantum Electron.* **2017**, *47*, 601. [[CrossRef](#)]
35. Yudin, N.N.; Khudoley, A.; Zinovev, M.; Slyunko, E.; Podzyvalov, S.; Kuznetsov, V.; Gorodkin, G.; Kumeysya, P.; Lysenko, A.; Kalsin, A.; et al. Experimental Investigation of Laser Damage Limit for ZPG Infrared Single Crystal Using Deep Magnetorheological Polishing of Working Surfaces. *Crystals* **2024**, *14*, 32. [[CrossRef](#)]
36. Bairamov, B.H.; Rud', V.Y. Properties of Dopants in ZnGeP₂, CdGeAs₂, AgGaS₂ and AgGaSe₂. *MRS Bull.* **1998**, *23*, 41–44. [[CrossRef](#)]
37. Yudin, N.; Zinoviev, M.; Kuznetsov, V.; Slyunko, E.; Podzyvalov, S.; Voevodin, V.; Lysenko, A.; Kalsin, A.; Shaimerdenova, L.; Baalbaki, H.; et al. Effect of Dopants on Laser-Induced Damage Threshold of ZnGeP₂. *Crystals* **2023**, *13*, 440. [[CrossRef](#)]
38. Vodopyanov, K.L.; Maffetone, J.P.; Zwieback, I.; Ruderman, W. AgGaS₂ optical parametric oscillator continuously tunable from 3.9 to 11.3 μm . *Appl. Phys. Lett.* **1999**, *75*, 1204–1206. [[CrossRef](#)]
39. Lippert, E.; Rustad, G.; Arisholm, G.; Stenersen, K. High power and efficient long wave IR ZnGeP₂ parametric oscillator. *Opt. Express* **2008**, *16*, 13878–13884. [[CrossRef](#)]
40. Antipov, O.; Novikov, A.; Eranov, I.; Kolker, D. High-efficiency oscillations at 1940 nm and 2070 nm in diode-pumped Tm:Lu₂O₃ ceramics lasers and their OPO frequency conversion. In Proceedings of the 2014 International Conference Laser Optics, St. Petersburg, Russia, 30 June–4 July 2014; p. 1. [[CrossRef](#)]

41. Das, S. Optical parametric oscillator: Status of tunable radiation in mid-IR to IR spectral range based on ZnGeP₂ crystal pumped by solid state lasers. *Opt. Quantum Electron.* **2019**, *51*, 70. [[CrossRef](#)]
42. Beasley, J.D. Thermal conductivities of some novel nonlinear optical materials. *Appl. Opt.* **1994**, *33*, 1000–1003. [[CrossRef](#)]
43. Eckardt, R.C.; Fan, Y.X.; Byer, R.L.; Marquardt, C.L.; Storm, M.E.; Esterowitz, L. Broadly tunable infrared parametric oscillator using AgGaSe₂. *Appl. Phys. Lett.* **1986**, *49*, 608–610. [[CrossRef](#)]
44. Isaenko, L.I.; Yelisseyev, A.P. Recent studies of nonlinear chalcogenide crystals for the mid-IR. *Semicond. Sci. Technol.* **2016**, *31*, 123001. [[CrossRef](#)]
45. Tyazhev, A.; Vedenyapin, V.; Marchev, G.; Isaenko, L.; Kolker, D.; Lobanov, S.; Petrov, V.; Yelisseyev, A.; Starikova, M.; Zondy, J.J. Singly-resonant optical parametric oscillation based on the wide band-gap mid-IR nonlinear optical crystal LiGaS₂. *Opt. Mater.* **2013**, *35*, 1612–1615. [[CrossRef](#)]
46. Morimoto, T.; Sono, N.; Miyamoto, T.; Kida, N.; Okamoto, H. Generation of a carrier-envelope-phase-stable femtosecond pulse at 10 μm by direct down-conversion from a Ti:sapphire laser pulse. *Appl. Phys. Express* **2017**, *10*, 122701. [[CrossRef](#)]
47. Kinyavetskiy, I.; Koribut, A.; Seleznev, L.; Klimachev, Y.; Dunaeva, E.; Ionin, A. Frequency conversion of a chirped Ti:sapphire laser pulse to 11.4 μm wavelength with SrMoO₄ Raman shifter and LiGaS₂ DFG crystal. *Opt. Laser Technol.* **2024**, *169*, 110035. [[CrossRef](#)]
48. Isaenko, L.; Dong, L.; Yelisseyev, A.; Lobanov, S.; Korzhneva, K.; Gromilov, S.; Sukhih, A.; Pugachev, A.; Vedenyapin, V.; Kurus, A.; et al. A new nonlinear optical crystal Li_{0.81}Ag_{0.19}InSe₂ with balanced properties for efficient nonlinear conversion in the mid-IR region. *J. Alloys Compd.* **2023**, *969*, 172382. [[CrossRef](#)]
49. Isaenko, L.; Dong, L.; Kurus, A.; Lin, Z.; Yelisseyev, A.; Lobanov, S.; Molokeev, M.; Korzhneva, K.; Goloshumova, A. Li_xAg_{1-x}GaSe₂: Interplay Between Lithium and Silver in Mid-Infrared Nonlinear Optical Chalcogenides. *Adv. Opt. Mater.* **2022**, *10*, 2201727. [[CrossRef](#)]
50. Lin, X.; Zhang, G.; Ye, N. Growth and Characterization of BaGa₄S₇: A New Crystal for Mid-IR Nonlinear Optics. *Cryst. Growth Des.* **2009**, *9*, 1186–1189. [[CrossRef](#)]
51. Badikov, V.; Badikov, D.; Shevyrdyaeva, G.; Tyazhev, A.; Marchev, G.; Panyutin, V.; Noack, F.; Petrov, V.; Kwasniewski, A. BaGa₄S₇: Wide-bandgap phase-matchable nonlinear crystal for the mid-infrared. *Opt. Mater. Express* **2011**, *1*, 316–320. [[CrossRef](#)]
52. Badikov, V.; Badikov, D.; Shevyrdyaeva, G.; Tyazhev, A.; Marchev, G.; Panyutin, V.; Petrov, V.; Kwasniewski, A. Phase-matching properties of BaGa₄S₇ and BaGa₄Se₇: Wide-bandgap nonlinear crystals for the mid-infrared. *Phys. Status Solidi RRL Rapid Res. Lett.* **2011**, *5*, 31–33. [[CrossRef](#)]
53. Yao, J.; Mei, D.; Bai, L.; Lin, Z.; Yin, W.; Fu, P.; Wu, Y. BaGa₄Se₇: A New Congruent-Melting IR Nonlinear Optical Material. *Inorg. Chem.* **2010**, *49*, 9212–9216. [[CrossRef](#)]
54. Yin, W.; Feng, K.; He, R.; Mei, D.; Lin, Z.; Yao, J.; Wu, Y. BaGa₂MQ₆ (M = Si, Ge; Q = S, Se): A new series of promising IR nonlinear optical materials. *Dalton Trans.* **2012**, *41*, 5653–5661. [[CrossRef](#)]
55. Lin, X.; Guo, Y.; Ye, N. BaGa₂GeX₆ (X = S, Se): New mid-IR nonlinear optical crystals with large band gaps. *J. Solid State Chem.* **2012**, *195*, 172–177. [[CrossRef](#)]
56. Badikov, V.V.; Badikov, D.V.; Laptev, V.B.; Mitin, K.V.; Shevyrdyaeva, G.S.; Shchebetova, N.I.; Petrov, V. Crystal growth and characterization of new quaternary chalcogenide nonlinear crystals for the mid-IR: BaGa₂GeS₆ and BaGa₂GeSe₆. *Opt. Mater. Express* **2016**, *6*, 2933–2938. [[CrossRef](#)]
57. Badikov, V.; Badikov, D.; Shevyrdyaeva, G.; Laptev, V.; Melnikov, A.; Chekalin, S. Optical and generation characteristics of new nonlinear Ba₂Ga₈GeS₁₆ and Ba₂Ga₈(GeSe₂)S₁₄ crystals for the mid-IR range. *Quantum Electron.* **2022**, *52*, 296. [[CrossRef](#)]
58. Badikov, V.V.; Badikov, D.V.; Shevyrdyaeva, G.S.; Kato, K.; Umemura, N.; Miyata, K.; Panyutin, V.L.; Petrov, V. Crystal growth and characterization of a new quaternary hexagonal nonlinear crystal for the mid-IR: Ba₂Ga₈GeS₁₆. *J. Alloys Compd.* **2022**, *907*, 164378. [[CrossRef](#)]
59. The optical properties of the nonlinear crystal BaGa₄Se₇. *Opt. Mater.* **2020**, *99*, 109564. [[CrossRef](#)]
60. Schunemann, P.G.; Zawilski, K.T. Horizontal Gradient Freeze Growth of Barium Thio- and Seleno-gallates for Mid-Infrared Frequency Conversion. In *High-Brightness Sources and Light-Driven Interactions*; Optica Publishing Group: Massachusetts, NW, USA, 2018; p. MT2C.7. [[CrossRef](#)]
61. Schunemann, P.G.; Zawilski, K.T. Seeded growth of BaGa₄S₇ and BaGa₄Se₇ for mid-IR frequency conversion. In *Optica Advanced Photonics Congress 2022*; Optica Publishing Group: Massachusetts, NW, USA, 2022; p. AM6A.2. [[CrossRef](#)]
62. Liu, B.W.; Zeng, H.Y.; Zhang, M.J.; Fan, Y.H.; Guo, G.C.; Huang, J.S.; Dong, Z.C. Syntheses, Structures, and Nonlinear-Optical Properties of Metal Sulfides Ba₂Ga₈MS₁₆ (M = Si, Ge). *Inorg. Chem.* **2015**, *54*, 976–981. [[CrossRef](#)] [[PubMed](#)]
63. *ANSI/IEEE Std. 176-1987*; IEEE Standard on Piezoelectricity. IEEE: Piscataway, NJ, USA, 1988. [[CrossRef](#)]
64. Petrov, V.; Badikov, V.V.; Badikov, D.V.; Kato, K.; Shevyrdyaeva, G.S.; Miyata, K.; Mero, M.; Wang, L.; Heiner, Z.; Panyutin, V.L. Barium nonlinear optical crystals for the mid-IR: Characterization and some applications. *J. Opt. Soc. Am. B* **2021**, *38*, B46–B58. [[CrossRef](#)]
65. Jiang, S.; Wan, S.; Luo, W.; Li, B.; Yao, J. The structural origin of the 15 μm residual absorption in the BaGa₄Se₇ crystal. *J. Mater. Chem. C* **2022**, *10*, 649–654. [[CrossRef](#)]
66. Kato, K.; Badikov, V.V.; Miyata, K.; Petrov, V. Refined Sellmeier equations for BaGa₄S₇. *Appl. Opt.* **2021**, *60*, 6600–6603. [[CrossRef](#)]
67. Yang, F.; Yao, J.Y.; Xu, H.Y.; Zhang, F.F.; Zhai, N.X.; Lin, Z.H.; Zong, N.; Peng, Q.J.; Zhang, J.Y.; Cui, D.F.; et al. Midinfrared Optical Parametric Amplifier With 6.4–11 μm Range Based on BaGa₄Se₇. *IEEE Photonics Technol. Lett.* **2015**, *27*, 1100–1103. [[CrossRef](#)]

68. Boursier, E.; Segonds, P.; Ménaert, B.; Badikov, V.; Panyutin, V.; Badikov, D.; Petrov, V.; Boulanger, B. Phase-matching directions and refined Sellmeier equations of the monoclinic acentric crystal BaGa₄Se₇. *Opt. Lett.* **2016**, *41*, 2731–2734. [[CrossRef](#)]
69. Kato, K.; Miyata, K.; Petrov, V. Phase-matching properties of BaGa₄Se₇ for SHG and SFG in the 0.901–10.5910 μm range. *Appl. Opt.* **2017**, *56*, 2978–2981. [[CrossRef](#)]
70. Zhai, N.; Li, C.; Xu, B.; Bai, L.; Yao, J.; Zhang, G.; Hu, Z.; Wu, Y. Temperature-Dependent Sellmeier Equations of IR Nonlinear Optical Crystal BaGa₄Se₇. *Crystals* **2017**, *7*, 62. [[CrossRef](#)]
71. Kato, K.; Miyata, K.; Petrov, V. Refined Sellmeier and thermo-optic dispersion formulas for BaGa₄Se₇. *Opt. Mater. Express* **2023**, *13*, 1852–1858. [[CrossRef](#)]
72. Kato, K.; Umemura, N.; Badikov, V.V.; Badikov, D.V.; Petrov, V. Temperature-dependent phase-matching properties of BaGa₂GeS₆ in the 0.767–10.5910 μm spectral range. *Appl. Opt.* **2022**, *61*, 10774–10777. [[CrossRef](#)]
73. Kato, K.; Miyata, K.; Badikov, V.V.; Petrov, V. Phase-matching properties of BaGa₂GeSe₆ for three-wave interactions in the 0.778–10.5910 μm spectral range. *Appl. Opt.* **2018**, *57*, 7440–7443. [[CrossRef](#)] [[PubMed](#)]
74. Kato, K.; Miyata, K.; Okamoto, T.; Badikov, V.V.; Petrov, V. Thermo-optic dispersion formula for BaGa₂GeSe₆. *Appl. Opt.* **2019**, *58*, 9709–9711. [[CrossRef](#)] [[PubMed](#)]
75. Kato, K.; Badikov, V.V.; Umemura, N.; Miyata, K.; Petrov, V. Phase-matching properties of Ba₂Ga₈GeS₁₆. *J. Opt. Soc. Am. B* **2023**, *40*, A17–A20. [[CrossRef](#)]
76. Guo, F.; Boursier, E.; Segonds, P.; Na, A.P.; Debray, J.; Badikov, V.; Panyutin, V.; Badikov, D.; Petrov, V.; Boulanger, B. Second-order nonlinear optical coefficients of the monoclinic crystal BaGa₄Se₇. *Opt. Lett.* **2022**, *47*, 842–845. [[CrossRef](#)] [[PubMed](#)]
77. Boursier, E.; Segonds, P.; Debray, J.; Inácio, P.L.; Panyutin, V.; Badikov, V.; Badikov, D.; Petrov, V.; Boulanger, B. Angle noncritical phase-matched second-harmonic generation in the monoclinic crystal BaGa₄Se₇. *Opt. Lett.* **2015**, *40*, 4591–4594. [[CrossRef](#)] [[PubMed](#)]
78. Kato, K.; Badikov, V.V.; Wang, L.; Panyutin, V.L.; Mitin, K.V.; Miyata, K.; Petrov, V. Effective nonlinearity of the new quaternary chalcogenide crystal BaGa₂GeSe₆. *Opt. Lett.* **2020**, *45*, 2136–2139. [[CrossRef](#)]
79. Sheik-bahae, M.; Said, A.A.; Stryland, E.W.V. High-sensitivity, single-beam n₂ measurements. *Opt. Lett.* **1989**, *14*, 955–957. [[CrossRef](#)] [[PubMed](#)]
80. Mero, M.; Wang, L.; Chen, W.; Ye, N.; Zhang, G.; Petrov, V.; Heiner, Z. Laser-induced damage of nonlinear crystals in ultrafast, high-repetition-rate, mid-infrared optical parametric amplifiers pumped at 1 μm. In *Pacific Rim Laser Damage 2019: Optical Materials for High-Power Lasers*; Shao, J., Jitsuno, T., Rudolph, W., Eds.; International Society for Optics and Photonics—SPIE: Cergy-Pontoise, France, 2019; Volume 11063, p. 1106307. [[CrossRef](#)]
81. Mero, M.; Petrov, V.; Heiner, Z. Progress in ultrafast, mid-infrared optical parametric chirped pulse amplifiers pumped at 1 μm. In *Nonlinear Frequency Generation and Conversion: Materials and Devices XIX*; Schunemann, P.G., Schepler, K.L., Eds.; International Society for Optics and Photonics—SPIE: Cergy-Pontoise, France, 2020; Volume 11264, p. 112640F. [[CrossRef](#)]
82. Yang, F.; Yao, J.Y.; Guo, Y.W.; Yuan, L.; Bo, Y.; Peng, Q.J.; Cui, D.F.; Wu, Y.C.; Xu, Z.Y. High-energy continuously tunable 8–14 μm picosecond coherent radiation generation from BGSe-OPA pumped by 1064 nm laser. *Opt. Laser Technol.* **2020**, *125*, 106040. [[CrossRef](#)]
83. Guo, Y.; Zhou, Y.; Lin, X.; Chen, W.; Ye, N. Growth and characterizations of BaGa₄S₇ crystal. *Opt. Mater.* **2014**, *36*, 2007–2011. [[CrossRef](#)]
84. Yao, J.; Yin, W.; Feng, K.; Li, X.; Mei, D.; Lu, Q.; Ni, Y.; Zhang, Z.; Hu, Z.; Wu, Y. Growth and characterization of BaGa₄Se₇ crystal. *J. Cryst. Growth* **2012**, *346*, 1–4. [[CrossRef](#)]
85. Exner, G.; Susner, M.A.; Murray, J.; Grigorov, A.; Siebenaller, R.; Conner, B.S.; Rowe, E.; Guha, S.; Petrov, V. Thermo-mechanical properties of BaGa₂GeS(e)₆ nonlinear optical crystals. *Opt. Mater. Express* **2023**, *13*, 1335–1344. [[CrossRef](#)]
86. Wu, J.; Huang, W.; Liu, H.g.; He, Z.; Chen, B.; Zhu, S.; Zhao, B.; Lei, Y.; Zhou, X. Investigation of the Thermal Properties and Crystal Growth of the Nonlinear Optical Crystals AgGaS₂ and AgGaGeS₄. *Cryst. Growth Des.* **2020**, *20*, 3140–3153. [[CrossRef](#)]
87. Aggarwal, R.L.; Fan, T.Y. Thermal diffusivity, specific heat, thermal conductivity, coefficient of thermal expansion, and refractive-index change with temperature in AgGaSe₂. *Appl. Opt.* **2005**, *44*, 2673–2677. [[CrossRef](#)]
88. Wei, J.; Murray, J.; Badikov, V.V.; Petrov, V.; Guha, S. Thermal Properties of the Trigonal Quaternary Nonlinear Crystals BaGa₂GeS₆ and BaGa₂GeSe₆. In *Proceedings of the Conference on Lasers and Electro-Optics, San Jose, CA, USA, 9–14 May 2021*; Optica Publishing Group: Massachusetts, NW, USA, 2021; p. STu1C.4. [[CrossRef](#)]
89. Zhang, Y.; Zuo, Y.; Li, Z.; Wu, B.; Yao, J.; Shen, Y. High energy mid-infrared laser pulse output from a BaGa₄Se₇ crystal-based optical parametric oscillator. *Opt. Lett.* **2020**, *45*, 4595–4598. [[CrossRef](#)] [[PubMed](#)]
90. Kostyukova, N.Y.; Boyko, A.A.; Badikov, V.; Badikov, D.; Shevyrdyaeva, G.; Panyutin, V.; Marchev, G.M.; Kolker, D.B.; Petrov, V. Widely tunable in the mid-IR BaGa₄Se₇ optical parametric oscillator pumped at 1064 nm. *Opt. Lett.* **2016**, *41*, 3667–3670. [[CrossRef](#)]
91. Exner, G.; Grigorov, A.; Badikov, V.; Petrov, V. Hardness and Young's modulus of BaGa₄S₇ and BaGa₄Se₇ nonlinear optical crystals. *Opt. Mater.* **2022**, *133*, 112994. [[CrossRef](#)]
92. Gupta, R.C.; Varshney, P.; Pravesh.; Lal, M.; Kumar, D.; Singh, K.; Verma, A. Mechanical stability parameters of chalcogenides and pnictides based optoelectronic materials. *Chalcogenide Lett.* **2023**, *20*, 101–112. [[CrossRef](#)]
93. *ISO 21254-1:2011; Lasers and Laser-Related Equipment—Test Methods for Laser-Induced Damage Threshold—Part 1: Definitions and General Principles*. International Organization for Standardization: Geneva, Switzerland, 2011.

94. Demos, S.G.; Hoffman, B.N.; Carr, C.W.; Cross, D.A.; Negres, R.A.; Bude, J.D. Mechanisms of laser-induced damage in absorbing glasses with nanosecond pulses. *Opt. Express* **2019**, *27*, 9975–9986. [[CrossRef](#)]
95. Liu, G.; Kuang, D.; Song, L.; Xu, C.; Yan, C. Mechanism in damage variation of nanosecond laser-induced damage of germanium sheets in vacuum. *Opt. Laser Technol.* **2023**, *157*, 108663. [[CrossRef](#)]
96. Stuart, B.C.; Feit, M.D.; Rubenchik, A.M.; Shore, B.W.; Perry, M.D. Laser-Induced Damage in Dielectrics with Nanosecond to Subpicosecond Pulses. *Phys. Rev. Lett.* **1995**, *74*, 2248–2251. [[CrossRef](#)]
97. Wood, R. Laser induced damage thresholds and laser safety levels. Do the units of measurement matter? *Opt. Laser Technol.* **1998**, *29*, 517–522. [[CrossRef](#)]
98. Manenkov, A.A.; Prokhorov, A.M. Laser-induced damage in solids. *Sov. Phys. Uspekhi* **1986**, *29*, 104. [[CrossRef](#)]
99. Bliss, E.S. Pulse duration dependence of laser damage mechanisms. *Opto-Electron.* **1971**, *3*, 99–108. [[CrossRef](#)]
100. Erushin, E.Y.; Kostyukova, N.Y.; Boyko, A.A.; Baranova, E.; Verbovaty, D.; Badikov, D. Issledovaniye luchevoy stoykosti serosoderzhashchikh kristallov bariyevykh khal'kogenidov. In Proceedings of the XIX International Youth Conference on Luminescence and Laser Physics, Irkutsk, Russia, 3–8 July 2023; p. 85.
101. Zhao, X.; Li, C.; Bai, J.; Wang, Z.; Yao, J.; Tan, R.; Xu, X. Recalibration of the nonlinear optical coefficients of BaGa₄Se₇ crystal using second-harmonic-generation method. *Opt. Lett.* **2021**, *46*, 5894–5897. [[CrossRef](#)]
102. Kostyukova, N.Y.; Boyko, A.A.; Eranov, I.D.; Antipov, O.L.; Kolker, D.B.; Kostyukov, A.I.; Erushin, E.Y.; Miroshnichenko, I.B.; Badikov, D.V.; Badikov, V.V. Laser-induced damage threshold of the nonlinear crystals BaGa₄Se₇ and BaGa₂GeSe₆ at 2091 nm in the nanosecond regime. *J. Opt. Soc. Am. B* **2020**, *37*, 2655–2659. [[CrossRef](#)]
103. Yuan, J.H.; Li, C.; Yao, B.Q.; Yao, J.Y.; Duan, X.M.; Li, Y.Y.; Shen, Y.J.; Wu, Y.C.; Cui, Z.; Dai, T.Y. High power, tunable mid-infrared BaGa₄Se₇ optical parametric oscillator pumped by a 2.1 μm Ho:YAG laser. *Opt. Express* **2016**, *24*, 6083–6087. [[CrossRef](#)] [[PubMed](#)]
104. Zhao, B.; Chen, Y.; Yao, B.; Yao, J.; Guo, Y.; Wang, R.; Dai, T.; Duan, X. High-efficiency, tunable 8–9 μm BaGa₄Se₇ optical parametric oscillator pumped at 2.1 μm. *Opt. Mater. Express* **2018**, *8*, 3332–3337. [[CrossRef](#)]
105. Zhang, J.; Wang, Q.; Hao, J.; Liu, H.; Yao, J.; Li, Z.; Liu, J.; Mak, K.F. Broadband, few-cycle mid-infrared continuum based on the intra-pulse difference frequency generation with BGSe crystals. *Opt. Express* **2020**, *28*, 37903–37909. [[CrossRef](#)]
106. Kostyukova, N.Y.; Boyko, A.A.; Erushin, E.Y.; Kostyukov, A.I.; Badikov, V.V.; Badikov, D.V.; Kolker, D.B. Laser-induced damage threshold of BaGa₄Se₇ and BaGa₂GeSe₆ nonlinear crystals at 1053 nm. *J. Opt. Soc. Am. B* **2019**, *36*, 2260–2265. [[CrossRef](#)]
107. Kolker, D.B.; Kostyukova, N.Y.; Boyko, A.A.; Badikov, V.V.; Badikov, D.V.; Shadrintseva, A.G.; Tretyakova, N.N.; Zenov, K.G.; Karapuzikov, A.A.; Zondy, J.J. Widely tunable (2.6–10.4 μm) BaGa₄Se₇ optical parametric oscillator pumped by a Q-switched Nd:YLiF₄ laser. *J. Phys. Commun.* **2018**, *2*, 035039. [[CrossRef](#)]
108. Yang, F.; Yong Yao, J.; Yan Xu, H.; Feng, K.; Long Yin, W.; Qin Li, F.; Yang, J.; Feng Du, S.; Jun Peng, Q.; Yuan Zhang, J.; et al. High efficiency and high peak power picosecond mid-infrared optical parametric amplifier based on BaGa₄Se₇ crystal. *Opt. Lett.* **2013**, *38*, 3903–3905. [[CrossRef](#)] [[PubMed](#)]
109. Boyko, A.A.; Eryshin, E.Y.; Kostyukova, N.Y.; Kolker, D.B.; Kostyukov, A.I.; Miroshnichenko, I.B.; Badikov, D.V.; Badikov, V.V. Laser-Induced Damage Threshold of dark yellow phase BaGa₄Se₇ Crystal at 1053 nm. In Proceedings of the 2020 International Conference Laser Optics (ICLO), St. Petersburg, Russia, 2–6 November 2020; p. 1. [[CrossRef](#)]
110. Erushin, E.; Kostyukova, N.; Boyko, A.; Loginova, A.; Safaraliev, G.; Shevyrdyaeva, G.; Badikov, D. Ba₂Ga₈GeS₁₆: New nonlinear optical crystals with high laser-induced damage threshold for parametric down-conversion in mid-IR. *Appl. Phys. B* **2023**, *130*, 10. [[CrossRef](#)]
111. Tyazhev, A.; Kolker, D.; Marchev, G.; Badikov, V.; Badikov, D.; Shevyrdyaeva, G.; Panyutin, V.; Petrov, V. Midinfrared optical parametric oscillator based on the wide-bandgap BaGa₄S₇ nonlinear crystal. *Opt. Lett.* **2012**, *37*, 4146–4148. [[CrossRef](#)]
112. Heiner, Z.; Petrov, V.; Mero, M. Efficient, sub-4-cycle, 1-μm-pumped optical parametric amplifier at 10 μm based on BaGa₄S₇. *Opt. Lett.* **2020**, *45*, 5692–5695. [[CrossRef](#)]
113. Zhang, J.J.; Yang, F.; Yang, S.D.; Fang, S.H.; Wang, X.J.; Peng, Q.J.; Ye, N.; Xu, Z.Y. Tunable mid-IR optical parametric amplifier pumped at 1064 nm based on a wideband-gap BaGa₄S₇ crystal. *Infrared Phys. Technol.* **2020**, *111*, 103571. [[CrossRef](#)]
114. Kostyukova, N.; Bobylev, A.; Boyko, A.; Zenov, K.; Shadrintseva, A.; Tretyakova, N.; Badikov, V.; Kolker, D. Wide tunable BaGa₄Se₇ optical parametric oscillator pumped by Nd:YLF laser. In Proceedings of the 2016 International Conference Laser Optics (LO), St. Petersburg, Russia, 27 June–1 July 2016; p. R8-39. [[CrossRef](#)]
115. Boyko, A.A.; Kostyukova, N.Y.; Badikov, V.; Badikov, D.; Panyutin, V.; Shevyrdyaeva, G.; Pasiskevicius, V.; Zukauskas, A.; Marchev, G.M.; Kolker, D.B.; et al. Intracavity difference-frequency mixing of optical parametric oscillator signal and idler pulses in BaGa₄Se₇. *Appl. Opt.* **2017**, *56*, 2783–2786. [[CrossRef](#)]
116. He, Y.; Xu, D.; Yao, J.; Wang, Y.; Guo, Y.; Zhu, X.; Yan, C.; Tang, L.; Li, J.; Zhong, K.; et al. Intracavity-Pumped, Mid-Infrared Tandem Optical Parametric Oscillator Based on BaGa₄Se₇ Crystal. *IEEE Photonics J.* **2019**, *11*, 1300109. [[CrossRef](#)]
117. Xu, W.T.; Wang, Y.Y.; Xu, D.G.; Li, C.; Yao, J.Y.; Yan, C.; He, Y.X.; Nie, M.T.; Wu, Y.C.; Yao, J.Q. High-pulse-energy mid-infrared optical parametric oscillator based on BaGa₄Se₇ crystal pumped at 1.064 μm. *Appl. Phys. B* **2017**, *123*, 80. [[CrossRef](#)]
118. Kang, M.; Deng, Y.; Yan, X.; Zeng, X.; Guo, Y.; Yao, J.; Zeng, F.; Zheng, J.; Zhou, K.; Qu, C.; et al. A compact and efficient 4.25 μm BaGa₄Se₇ optical parametric oscillator. *Chin. Opt. Lett.* **2019**, *17*, 121402. [[CrossRef](#)]
119. Xu, D.; Zhang, J.; He, Y.; Wang, Y.; Yao, J.; Guo, Y.; Yan, C.; Tang, L.; Li, J.; Zhong, K.; et al. High-energy, tunable, long-wave mid-infrared optical parametric oscillator based on BaGa₄Se₇ crystal. *Opt. Lett.* **2020**, *45*, 5287–5290. [[CrossRef](#)] [[PubMed](#)]

120. Bian, J.; Kong, H.; Ye, Q.; Yao, J.; Guo, L.; Sun, X. Narrow-linewidth BaGa4Se7 optical parametric oscillator. *Chin. Opt. Lett.* **2022**, *20*, 041901. [[CrossRef](#)]
121. Liu, G.; Zhang, Z.; Li, C.; Meng, J.; Li, T.; Zhao, Z.; Cong, Z.; Yao, J.; Liu, Z. Comparison of a high-power 3.75 μm BaGa4Se7 OPO based on a plane-parallel resonator and an unstable resonator with a Gaussian reflectivity mirror. *Appl. Opt.* **2022**, *61*, 7330–7335. [[CrossRef](#)] [[PubMed](#)]
122. He, Y.; Yan, C.; Chen, K.; Xu, D.; Li, J.; Zhong, K.; Wang, Y.; Yao, R.; Yao, J.; Yao, J. High Repetition Rate, Tunable Mid-Infrared BaGa4Se7 Optical Parametric Oscillator Pumped by a 1 μm Nd:YAG Laser. *Appl. Sci.* **2022**, *12*, 7197. [[CrossRef](#)]
123. Kang, M.; Deng, Y.; Yao, J.; Zhu, Q. High Power and Efficient 4.43 μm BaGa4Se7 Optical Parametric Oscillator Pumped at 1064 nm. *Photonics* **2022**, *9*, 105. [[CrossRef](#)]
124. Ye, Q.; Kong, H.; Bian, J.; Yao, J.; Wang, E.; Wu, Y.; Xu, H.; Wen, K.; Hu, Y. Widely tunable and high resolution mid-infrared laser based on BaGa4Se7 optical parametric oscillator. *Front. Optoelectron.* **2023**, *16*, 26. [[CrossRef](#)]
125. Wen, N.; Shen, Y.; Wen, Y.; Wang, E.; Yao, J.; Fang, Y.; Gao, H.; Bo, Y.; Chen, Z.; Peng, Q. A Stable and Compact Mid-IR at 6.45 μm Exceeding 6 mJ of Pulse Energy BaGa4Se7 Optical Parametric Oscillator. *Appl. Sci.* **2023**, *13*, 6413. [[CrossRef](#)]
126. Liu, G.; Chen, Y.; Li, Z.; Yang, K.; Yao, B.; Yao, J.; Wang, R.; Yang, C.; Mi, S.; Dai, T.; et al. High-beam-quality 2.1 μm pumped mid-infrared type-II phase-matching BaGa4Se7 optical parametric oscillator with a ZnGeP2 amplifier. *Opt. Lett.* **2020**, *45*, 3805–3808. [[CrossRef](#)]
127. Yang, K.; Liu, G.; Li, C.; Yao, B.; Yao, J.; Chen, Y.; Mi, S.; Duan, X.; Dai, T. Research on performance improvement technology of a BaGa4Se7 mid-infrared optical parametric oscillator. *Opt. Lett.* **2020**, *45*, 6418–6421. [[CrossRef](#)] [[PubMed](#)]
128. Hu, S.; Wang, L.; Guo, Y.; Cheng, T.; Wu, X.; Wang, Z.; Wu, H.; Yao, J.; Wu, Y.; Jiang, H. High-conversion-efficiency tunable mid-infrared BaGa4Se7 optical parametric oscillator pumped by a 2.79 μm laser. *Opt. Lett.* **2019**, *44*, 2201–2203. [[CrossRef](#)] [[PubMed](#)]
129. Jelínek, M.; Kubeček, V.; Novák, O.; Huynh, J.; Cimrman, M.; Chyla, M.; Smrž, M.; Mocek, T.; Smetanin, S.N.; Grechin, S.G.; et al. Difference Frequency Generation in BaGa4Se7 Tunable in a 6.5–8.5 μm Range with a Peak Power of 30 MW Pumped by 1.03 μm , 1.8 ps Laser. In *Optica High-brightness Sources and Light-Driven Interactions Congress 2022*; Optica Publishing Group: Massachusetts, NW, USA, 2022; p. JTh4A.15. [[CrossRef](#)]
130. Tian, K.; Wang, W.; Li, C.; Wan, Z.; Hu, B.; He, L.; Xiang, M.; Yao, J.; Wu, H.; Liang, H. Ultrabroad (3.7–17 μm) tunable femtosecond optical parametric amplifier based on BaGa4Se7 crystal. *Opt. Lett.* **2022**, *47*, 5973–5976. [[CrossRef](#)] [[PubMed](#)]
131. Lukošiusas, J.; Kananavičius, R.; Danilevičius, R.; Januškevičius, R.; Schunemann, P.G.; Michailovas, A. Efficient high resolution broadband SFG spectrometer utilizing BGSe nonlinear crystal covering 2.5–10 μm spectral range. In *Laser Congress 2023 (ASSL, LAC)*; Optica Publishing Group: Massachusetts, NW, USA, 2023; p. Ath2A.4. [[CrossRef](#)]
132. Sun, M.G.; Cao, Z.S.; Yao, J.Y.; Ma, H.L.; Guo, Y.W.; Gao, X.M.; Rao, R.Z.; Wu, Y.C. Continuous-wave difference-frequency generation based on BaGa4Se7 crystal. *Opt. Express* **2019**, *27*, 4014–4023. [[CrossRef](#)]
133. Boyko, A.; Badikov, V.; Shevyrdyaeva, G.; Badikov, D.; Pasiskevicius, V.; Zukauskas, A.; Petrov, V. Intracavity-pumped, cascaded optical parametric oscillator based on BaGa2GeSe6. In *High-Brightness Sources and Light-Driven Interactions*; Optica Publishing Group: Massachusetts, NW, USA, 2018; p. MW2C.3. [[CrossRef](#)]
134. Chen, W.; Wang, L.; Divliansky, I.B.; Pasiskevicius, V.; Mhibik, O.; Moelster, K.M.; Zukauskas, A.; Glebov, L.B.; Petrov, V. Narrowband, intracavity-pumped, type-II BaGa2GeSe6 optical parametric oscillator. *Opt. Express* **2024**, *32*, 1728–1735. [[CrossRef](#)]
135. Elu, U.; Maidment, L.; Vamos, L.; Steinle, T.; Haberstroh, F.; Petrov, V.; Badikov, V.; Badikov, D.; Biegert, J. Few-cycle mid-infrared pulses from BaGa2GeSe6. *Opt. Lett.* **2020**, *45*, 3813–3815. [[CrossRef](#)]
136. Stibenz, G.; Beutler, M.; Rimke, I.; Badikov, V.; Badikov, D.; Petrov, V. Femtosecond mid-IR difference-frequency generation in BaGa2GeSe6 from a 40 MHz optical parametric oscillator pumped at 1035 nm. In *Conference on Lasers and Electro-Optics*; Optica Publishing Group: Massachusetts, NW, USA, 2018; p. STh4F.5. [[CrossRef](#)]
137. Ionin, A.A.; Badikov, D.V.; Badikov, V.V.; Kinyaevskiy, I.O.; Klimachev, Y.M.; Kotkov, A.A.; Kozlov, A.Y.; Sagitova, A.M.; Sinitsyn, D.V. Sum frequency generation of multi-line slab radio frequency discharge carbon monoxide laser system with intracavity nonlinear BaGa2GeSe6 crystal. *Opt. Lett.* **2018**, *43*, 4358–4361. [[CrossRef](#)]

Disclaimer/Publisher's Note: The statements, opinions and data contained in all publications are solely those of the individual author(s) and contributor(s) and not of MDPI and/or the editor(s). MDPI and/or the editor(s) disclaim responsibility for any injury to people or property resulting from any ideas, methods, instructions or products referred to in the content.